# A model to better understand the role of mechanical stimuli in regulating cell fate during osteochondral defect repair


## Abstract

In a previous study, we developed a computational mechanobiological model to explore the role of substrate stiffness and local oxygen availability in regulating cell fate during spontaneous osteochondral defect repair. While this model successfully simulated many aspects of the regenerative process, it was unable to predict the spatial pattern of bone formation observed during the latter stages of the repair process. The objective of this study was, therefore, to investigate the role of tissue strain in regulating the spatial and temporal patterns of stem cell differentiation during spontaneous osteochondral defect repair. Motivated by the findings of a number of prior *in vitro* studies, our computational mechanobiological model was updated to include rules based on the hypothesis that chondrocyte hypertrophy and endochondral ossification were inhibited in regions of high strain. The model also considered the hypothesis that excessively high magnitudes of local strain result in the formation of mechanically inferior fibrocartilage. These rules were first developed by attempting to simulate stem cell differentiation within an *in vitro* bioreactor system which was capable of controlling the levels of oxygen and mechanical cues within MSC-laden hydrogels. The updated model was able to predict the experimentally observed behaviour whereby the groups which were subjected to dynamic compression presented a reduction in chondrocyte hypertrophy and calcific deposition. Following this, the updated model was then used to simulate the pattern of tissue formation which had been experimentally observed during spontaneous osteochondral defect repair. As well as correctly predicting the spatial pattern of bone formation, the updated model also provided insights into the role that the mechanical environment plays on the spontaneous repair process; namely, that oxygen regulates endochondral ossification during the early phases of repair, while, during the latter stages, mechanics plays a key role in directing this process.

# 1 Introduction

Osteochondral defects of a certain size have the capacity to repair spontaneously [1]. This reparative response is mediated, at least in part, by mesenchymal stem cells (MSCs) which migrate from the bone marrow to the site of injury [2]. This reparative process forms the basis of a number of different surgical strategies designed to treat both osteochondral and chondral defects [3,4]. All of the current options, however, have limited success in the long term, as the repair tissue which initially forms breaks down over time [3]. In order to design novel tissue engineering strategies to overcome these issues, a better understanding of the factors which affect the formation of the repair tissue, as well as its subsequent failure, are required. To this end, we have recently developed a computational model of the spontaneous repair process within an osteochondral defect. The model made use of a previously developed tissue differentiation algorithm where MSC fate was governed by the local oxygen tension and stiffness of the surrounding substrate. While this model provided insight into the role that angiogenesis plays in the repair process, it was unable to predict the spatial formation of bone which has been experimentally observed during the latter stages of repair [5]. In addition to this, it did not account for the putative role that mechanical loading plays in the outcome of osteochondral defect repair. This may explain its inability to accurately predict the patterns of tissue formation observed in the latter stages of the regenerative process whereby cartilage is converted into bone through the process of endochondral ossification.

Mechanical loading has long been implicated in directing tissue formation, and in particular, cartilage formation during osteochondral defect repair [6–10]. Numerous studies have examined the effect that the magnitude and type of loading has on the repair tissue which forms within osteochondral defects [7–10]. In general it has been shown that active loading applied at an early stage leads to the formation of fibrous tissue and fibrocartilage, while continuous passive motion has been shown to result in the formation of hyaline cartilage [7,8,11]. A number of *in vitro* studies, where the levels of mechanical stimulation can be carefully controlled using bioreactor systems, have also demonstrated how compressive loading can regulate chondrogenesis of MSCs [12–16]. For example, Thorpe *et al.* [17] showed that dynamic compressive loading of chondrogenically primed MSCs led to the upregulation of chondrogenic markers and also inhibited terminal differentiation and mineralisation. These findings suggest that mechanics plays a key role in regulating hypertrophy and endochondral ossification of cartilage. In addition, numerous *in vitro* studies have shown that MSCs exposed

to high magnitudes of dynamic tensile strain, when maintained in chondrogenic media, display markers of fibrocartilage [18–20].

Based on these studies, we sought to improve our previous model of stem cell differentiation by implementing a series of rules whereby the local mechanical environment affects the fate of the cartilaginous tissue formed in damaged bones or joints. In particular we hypothesised that during the spontaneous repair process, tissue level strains regulate chondrocyte hypertrophy and the rate of endochondral ossification, and that excessive local strain promotes the formation of fibrocartilage. In the first part of this study, a rule was implemented into the model whereby chondrocyte hypertrophy and endochondral ossification were inhibited in regions of high (> 5 %) octahedral shear strain. This was developed by modelling the findings of the *in vitro* bioreactor study conducted by Thorpe *et al.* [17], who modulated the levels of strain and oxygen through the depth of MSC-laden hydrogels. We then tested the predictive capacity of this updated model by attempting to simulate the time-course of the spontaneous repair process within an osteochondral defect. In the final part of the study an additional rule was developed whereby high magnitudes of octahedral shear strain (> 10 %), within an otherwise chondrogenic environment, leads to the formation of fibrocartilage.

# 2 Method

## 2.1 *In vitro* experiment to be simulated

The details of this experiment are described in elsewhere [17]. Briefly, porcine MSCs were seeded at a density of 20 x $10^3$ cells/$mm^3$ in cylindrical, 2 % agarose hydrogels of dimensions ϕ 6 mm x 4 mm. Constructs were cultured in chondrogenic media for 21 days before being split into an unconfined and a confined group which were then cultured for a further 3 weeks. The confined group were press-fitted in a PTFE chamber which served to confine the bottom half of the construct. During this time constructs from both groups either remained under free swelling conditions (FS) or were subjected to dynamic compression (DC) at an amplitude of 10 % strain and a frequency of 1 Hz for 4 hours per day, 5 day per week. Following culture, among other tests, histology and immunohistochemistry were performed to determine the spatial calcific deposition within the MSC-laden hydrogel. This was deemed to be indicative of chondrocyte hypertrophy. In addition to this, the oxygen tension was measured through

the depth of the constructs after 4 days of culture in both the confined and unconfined groups, using fibre optic oxygen microsensors. The results of this were then used in conjunction with a computational model to determine the Michealas-Menten parameters for the differentiated cells.

## 2.2 Finite Element Models

Three-dimensional Finite Element (FE) models were used to determine the biophysical stimuli generated in the cell-seeded constructs which were exposed to DC within the bioreactor system described above, as well as in an osteochondral defect. Both sets of models were implemented in the open source FE package FEBio (version 2.0, University of Utah, Technology Commercialization Office, 615 Arapeen Drive, Suite 310, Salt Lake City). All of the materials used in the models were bi-phasic and the material properties of each tissue type used are listed in **Error! Reference source not found.**. The model was run using an iterative procedure (Supplementary Material 8.1) and at the end of each iteration the material properties were updated based on the results of the cell differentiation algorithm described below. The new parameters were calculated using a rule of mixtures in conjunction with a temporal smoothing procedure [21].

*Table 1: Material Parameters*

| Material Property | Granulation Tissue | Fibrous Tissue | Fibro-Cartilage | Cartilage | Hypertrophic Cartilage | Immature Bone | Mature Bone | Cortical Bone |
|---|---|---|---|---|---|---|---|---|
| Young's Modulus (MPa) | 1[a] | 2[a,b] | 5 | 10[a,b] | 20 | 1000[a] | 6000[c] | 20,000[c] |
| Poisson's Ratio | 0.167 | 0.167 | 0.167 | 0.167 | 0.167 | 0.3 | 0.3 | 0.3 |
| Permeability ($mm^4$/ Ns) | 0.01[a] | 0.01[a,b] | 0.01 | 0.005[a,b] | 0.005 | 0.1[a] | 0.37[d] | 1e-5[a] |
| Solid Volume Fraction | 0.2 | 0.2 | 0.2 | 0.2 | 0.2 | 0.2 | 0.2 | 0.2 |

a 22

b 23

c 24

d25

### 2.2.1 *In Vitro* Model

Three Dimensional Finite Element models were developed for both the unconfined and the confined groups (Figure 1). Both models had a geometry of ϕ 6 mm x 4 mm and, using symmetry, were simplified to depict a quarter of the construct as it was revolved around the centre axis. For the confined group the confinement chamber was implemented using a sliding contact interface between the construct and the chamber. In both models a 10 %

compressive strain was applied to the top surface of the construct over a period of 0.5 s. At the onset of loading, the material parameters for cartilage were used, based on the assumption that chondrogenic differentiation had occurred (Table 1).

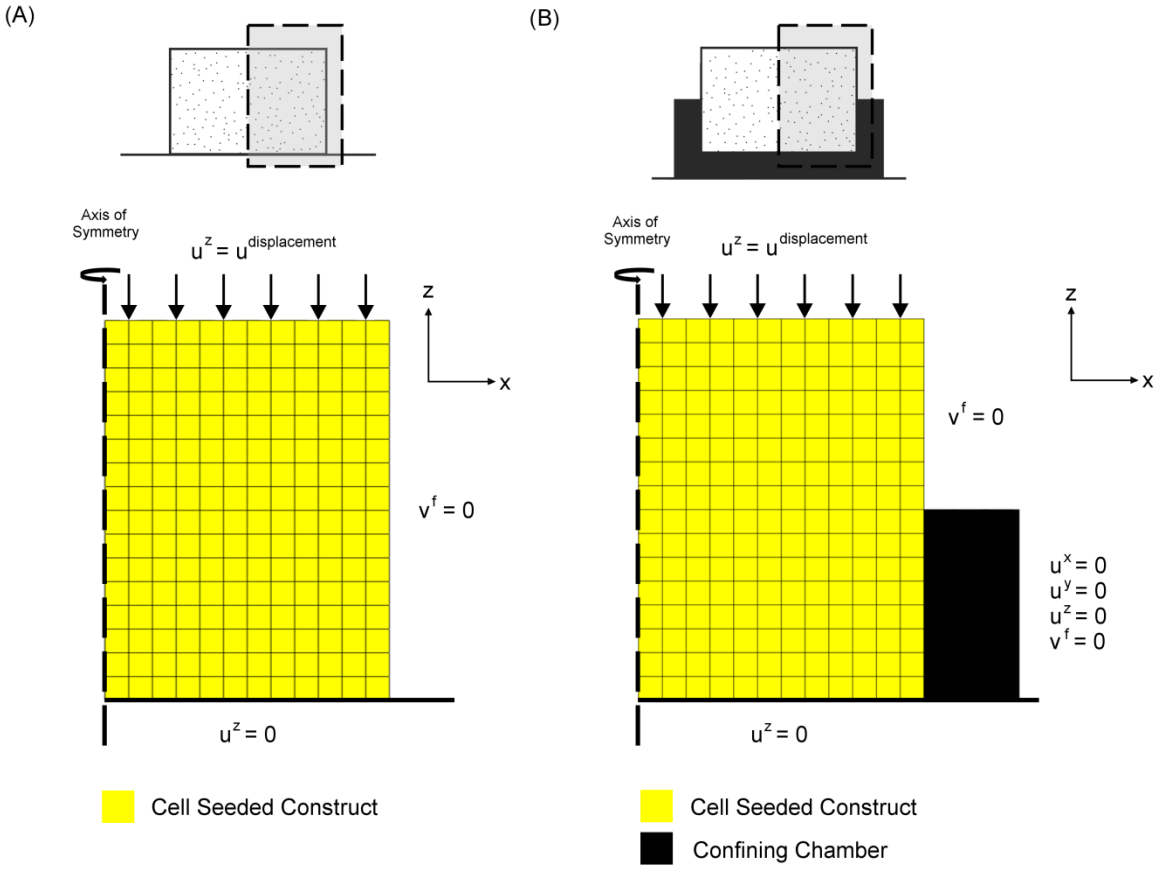


*Figure 1: FE Model and boundary conditions for the (A) Unconfined and (B) Confined in-vitro simulations. Displacement in the x and z directions and fluid velocity are shown as $u^x$, $u^z$ and $v^f$ respectively.*

### 2.2.2 Osteochondral Defect

A simplified 3D FE model of an osteochondral defect within the femoral condyle was developed (Figure 2). Similar to previous studies [26–28], the condyle was modelled as a flattened semi-sphere of radius 20 mm, consisting of a 1 mm-deep layer of cortical bone which overlaid mature cancellous bone. The condyle was covered with a 2 mm-thick layer of cartilage which was supported by the meniscus. The tibial plateau was modelled as a rigid contact layer, the permeability of which was assumed to be the same as cartilage. Due to convergence issues, the meniscus was treated as a solid material where a sliding interface was used to model the contact between it and the cartilage layer. This was treated as a transversely isotropic elastic material with a higher stiffness in the circumferential direction ($E^x = E^z = 20$ MPa; $E^y = 140$ MPa; $v^{xy} = 0.2$; $v^{yz} = 0.49$; $G^{xy} = 50$ MPa) [28,29]. At the centre of the FE model, a defect of size $\varphi$

5 mm x 5 mm was included. This was assumed to be initially filled with granulation tissue. A load of 2400 N was applied over 1 second, based on the assumption of five to six times subject weight (80 kg) spread evenly between the lateral and medial compartments [30].

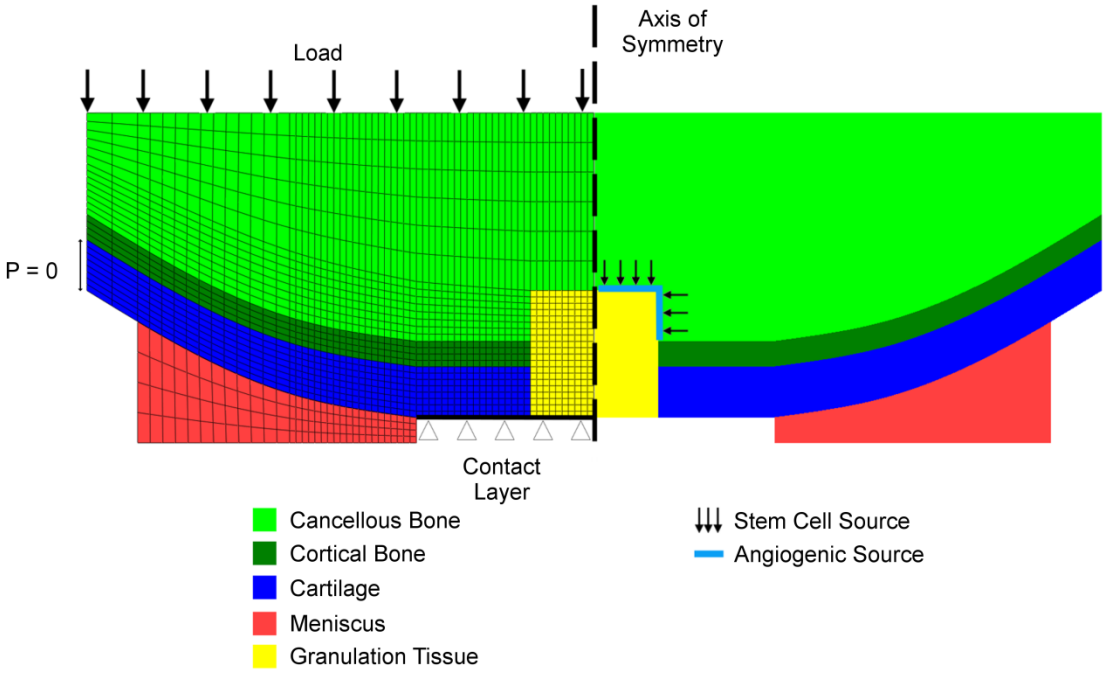


*Figure 2: FE model and boundary conditions for the osteochondral defect simulations.*

## 2.3 Angiogenesis

Angiogenesis was only considered in the osteochondral defect model. This was implemented using a lattice-based approach whereby the elements of the FE model were discretised into a sequence of lattice points, each of which represented a potential cell space [31]. Each lattice point had a diameter of 10 µm which corresponded with an overall lattice density of 1 x $10^6$ lattice points/$mm^3$. Blood vessels were then modelled as a sequence of adjoining lattice points, each of which represented an endothelial cell (EC) within a microvessel. Vessels were programmed to stop growing if the octahedral shear strain in the element exceeded a threshold limit ($\varepsilon^{octahedral} > \varepsilon^{angio}$). Vessels were also able to branch should their length exceed a certain value ($L_{min}$). The probability of branching then increased linearly until the vessel reached the maximum allowable length ($L_{max}$), at which point the probability of branching occurring was 1 [31]. If two vessels crossed the same path, anastomosis occurred and the two vessels fused together. As an extension of our previous model, and similar to the method described by Carlier *et al.* [32], it was assumed that blood and nutrients could only flow through vessels which had formed a closed loop. Based on this, the ECs which

made up a blood vessel were considered inactive until anastomosis had occurred. The effect of this updated model on the predicted outcome of tissue formation was examined by comparing the simulation results from the previous model (where all vessels were considered active) with those obtained using the new model (Supplementary Material 8.2).

Vessels grew at a constant rate ($V^{growth}$) and could grow into any neighbouring lattice point, provided that it was empty. Vessel direction was governed using strain-dependent rules which were developed by simulating [33] the *in vitro* study conducted by Matsumoto *et al.* [34]. In these studies it was shown that, when cultured in 2D, endothelial cell migration was biased in the direction perpendicular to the applied strain. Following from this, it was hypothesised that, within a 3D environment, EC cells either align themselves in the direction perpendicular to the maximum principal strain or in the direction of the minimum principal strain (Burke & Kelly, 2014). In the developed model it was assumed that the latter was case, and as such, there were three potential options which determined the vessel direction: 1) continue growing in the previous direction; 2) move in the direction of minimum principal strain or; 3) move in a random direction. The probability that a vessel would continue to grow in the same direction as the previous iteration ($P^{prev}$) was 0.4. The probability that a vessel would grow in the direction of the minimum principal strain ($P^{strain}$) was dependent upon the absolute magnitude of the strain. This was calculated using a simple linear model where $P^{strain} = 0$ at $\boldsymbol{\varepsilon}^{min} = 0$ up to maximum of $P^{strain} = 0.6$ at $|\boldsymbol{\varepsilon}^{min}| \geq 0.18$. The final case where a vessel grew in a random direction was dictated by the remaining probability ($1 - P^{prev} - P^{strain}$).

At day 0, it was assumed that vessels grew into the callus from the exposed cancellous bone (Figure 1). This assumption is based on the findings that this tissue is highly vascularised and provides a nutrient supply to both itself and the articular cartilage [3]. The initial number of vessels was governed by the parameter $N^{angio}$ which denoted the proportion of lattice points on the cancellous bone surfaces which were invading blood vessels.

*Table 2: Angiogenesis and MSC Differentiation Model Parameters*

| Model Parameter | Symbol | Source | Unit | Value |
|---|---|---|---|---|
| **Octahedral shear strain threshold for inhibition of angiogenesis** | $\varepsilon^{angio}$ | Estimated | - | 0.1 |
| **Blood vessel growth rate** | $V^{growth}$ | Estimated | mm $day^{-1}$ | 0.1 |
| **Minimum length for branching** | $L_{min}$ | [31] | Mm | 0.2 |
| **Maximum length without branching** | $L_{max}$ | [31] | Mm | 0.5 |
| **Minimum cell age for MSC differentiation** | $Age^{cell}$ | Estimated | days | 5 |
| **Oxygen diffusion coefficient** | G | [21,35] | $mm^2$ $s^{-1}$ | 2.2E-03 |
| **Initial oxygen tension** | $O_2^{initial}$ | [36] | mol $mm^{-3}$ | 101.6E-12 |
| **Oxygen tension for inhibition of differentiation** | $O_2^{inhibition}$ | [37] | mol $mm^{-3}$ | 5E-12 |
| **Oxygen limit for cartilage** | $O_2^{cartilage}$ | [21] | mol $mm^{-3}$ | 30E-12 |
| **Oxygen limit for differentiation of cartilage to hypertrophic cartilage** | $O_2^{hypertrophic}$ | Estimated | mol $mm^{-3}$ | 30E-12 |
| **Oxygen limit for calcification of hypertrophic cartilage** | $O_2^{endochondral}$ | Estimated | mol $mm^{-3}$ | 50.48E-12 |

## 2.4 Cell Migration, Cell Proliferation and Cell Death

The migration and proliferation of MSCs, osteoblasts (OBs), chondrocytes (CCs), fibroblasts (FBs), hypertrophic chondrocytes (HC) and fibrochondrocytes (FCs) was also modelled using a lattice approach [31,38]. The migration of cells was implemented using 'random walk' theory [38]. Cell proliferation was implemented in a similar fashion, provided that there was a vacant position beside the parent cell. Cell proliferation was inhibited in regions where the oxygen concentration fell below a specific threshold value ($O_2^{prolif}$) (**Error! Reference source not found.**). The maximum number of cells allowed in any element was limited to $1 \times 10^5$ cells/$mm^3$ [21]. The migration rate ($M$) determined the number of attempted migration actions per time step while the doubling time ($DT$) was the age a cell had to be before it proliferated (Table 3). It was assumed that 5 % of the lattice points on the cancellous surface of the defect (Figure 2) and 0.5 % of the interior lattice points contained MSCs at day 0. If the oxygen concentration fell below a threshold value ($O_2^{death}$) then cell death was initiated.

## 2.5 Oxygen Transport

Oxygen transport was modelled using the FE package COMSOL Multiphysics (version 4.3). For both the *in vitro* and *in vivo* simulations the same mesh was used for oxygen transport as was used for the stiffness models (**Error! Reference source not found.**). The governing equation (Equation 1) was updated during each iteration based on the number of each cell type in a specific element. In this case the oxygen consumption term was updated based on the number of MSCs, CCs, OBs, FBs and HCs, while the oxygen production term was determined based on the number of active ECs. In the case of the *in vitro* simulations, the oxygen production term was not implemented as blood vessel formation was not considered.

$$\frac{dO_2}{dt} = G\nabla^2 O_2 - \sum_{n=1}^{6} \rho_n \frac{Q^{max,n} O_2}{K^{m,n} + O_2} + Q^{vessels}$$

Equation 1

The oxygen diffusion coefficient G = 2.2 x $10^{-3}$ $mm^2$ $s^{-1}$. Oxygen consumption was modelled separately for each cell phenotype using Michealas-Menten kinetics [39–41]. In the equation shown, each phenotype was represented by n, whereby n = 1 represents MSCs; n = 2 represents CCs; n = 3 represents OBs; n = 4 represents FBs; n = 5 represents AB and; n = 6 represents HCs (**Error! Reference source not found.**). For each cell type: $\rho_n$ was the number of cells in the element; $Q^{max,n}$ was the maximum oxygen consumption; and $K^{m,n}$ was the oxygen consumption at half maximum concentration.

The oxygen supply from the blood vessels within each element was modelled with $Q^{vessels}$ which was calculated using the relationship outlined in equation 2.

$$Q^{vessels} = \begin{cases} \frac{O_2^{vessels} - O_2}{K^{vessels}}, & O_2 < O_2^{vessels} \\ 0, & O_2 \geq O_2^{vessels} \end{cases}$$

In this case $K^{vessels}$ is a temporal smoothing term used to prevent irregular jumps in the oxygen concentration ($K^{vessels}$ = 10 s) while $O_2^{vessels}$ was the minimum oxygen concentration within the element. $O_2^{vessels}$ was determined as a function of $v^{density}$ which in turn was the percentage of lattice points within the element which contained active ECs. A linear relationship was used to calculate $O_2^{vessels}$ where $O_2^{vessels}$ = 0 mol/$mm^3$ for $v^{density}$ = 0 up to a maximum of $O_2^{vessels}$ = 101.6 x $10^{-12}$ mol/$mm^3$ at $v^{density,\ max}$.

For the *in vivo* simulations, in accordance with the fact that cancellous bone is highly vascularised [3], it was assumed that there was a constant oxygen tension of 10 % at the

exposed bone within the defect. In addition to this a constant oxygen boundary condition of 5 % was applied to the surface of the defect in order to simulate the nutrient supply from the synovial fluid [41,42]. Finally, based on the *in silico* study conducted by Zhou *et al.* [41], the following three assumptions were made: 1) The synovial fluid was well mixed and as such any gradients within the fluid were negligible 2) Oxygen transport was steady-state, meaning that the effects of mechanical loading and cartilage deformation on oxygen transport were ignored 3) Gradients from the cell surface to the bulk tissue were negligible.

For the *in vitro* simulations, in accordance with the experimental results of Thorpe *et al.* [17], a constant oxygen boundary condition of 101.6 x $10^{-12}$ mol $mm^{-3}$ (10 %) was applied at the exposed surfaces of the gel. Furthermore, based on the experimentally measured values for the Michealas-Menten parameters derived in the same study, in the *in vitro* simulations $q^{max}$ = 48.6 x $10^{-15}$ mol $cell^{-1}$ $s^{-1}$ and $K^m$ = 5 x $10^{-11}$ mol $mm^{-3}$.

*Table 3: Cell Model Parameters*

| Model Parameter | MSC | CC | OB | FB | HC | FC |
|---|---|---|---|---|---|---|
| Doubling Time [days] | 0.5[a] | 1.5[a] | 1[a] | 0.5[a] | 1.5[a] | 1.5 |
| Migration Rate [µm/hr] | 26.6[c] | N/A | N/A | 26.6[c] | N/A | N/A |
| Anoxic Death Rate [% cells $day^{-1}$] | 20 | 20 | 20 | 20 | 20 | 20 |

a43

b44

c45

*Table 4: Oxygen parameters for each cell phenotype*

| Michealas - Menten Parameters | MSC | CC | OB | FB | HC | FC |
|---|---|---|---|---|---|---|
| Cell type (n) | 1 | 2 | 3 | 4 | 5 | 6 |
| Max Consumption Rate ($Q_{max}$) [mol $cell^{-1}$ $hr^{-1}$] | 93.2 x$10^{-15}$ [a] | 1.8 x$10^{-15}$ [a, b] | 93.2 x$10^{-15}$ [a] | 93.2 x$10^{-15}$ [a] | 1.8 x$10^{-15}$ [a] | 1.8 x$10^{-15}$ [a, b] |
| Oxygen Concentration at half max consumption [mol $mm^{-3}$] | 22.5 x$10^{-12}$ | 22.5 x$10^{-12}$ | 22.5 x$10^{-12}$ | 22.5 x$10^{-12}$ | 22.5 x$10^{-12}$ | 22.5 x$10^{-12}$ |
| Oxygen Concentration for cell proliferation ($O2_{prolif}$) [mol $mm^{-3}$] | 40 x$10^{-12}$ [a] | 10 x$10^{-12}$ | 80 x$10^{-12}$ [a] | 20 x$10^{-12}$ | 30 x$10^{-12}$ | 10 x$10^{-12}$ |
| Oxygen Concentration for cell death ($O2_{death}$) [mol $mm^{-3}$] | 5 x$10^{-12}$ | 5 x$10^{-12}$ | 20 x$10^{-12}$ | 5 x$10^{-12}$ | 5 x$10^{-12}$ | 5 x$10^{-12}$ |

a 32

b 46

## 2.6 MSC Differentiation and Chondrocyte Hypertrophy

The rules governing MSC differentiation are outlined in detail elsewhere [21] and are graphically depicted in Figure 3B. Based on the assumption that the stiffness of the

granulation tissue is not low enough to facilitate adipogenesis, this was not considered in the osteochondral defect model.

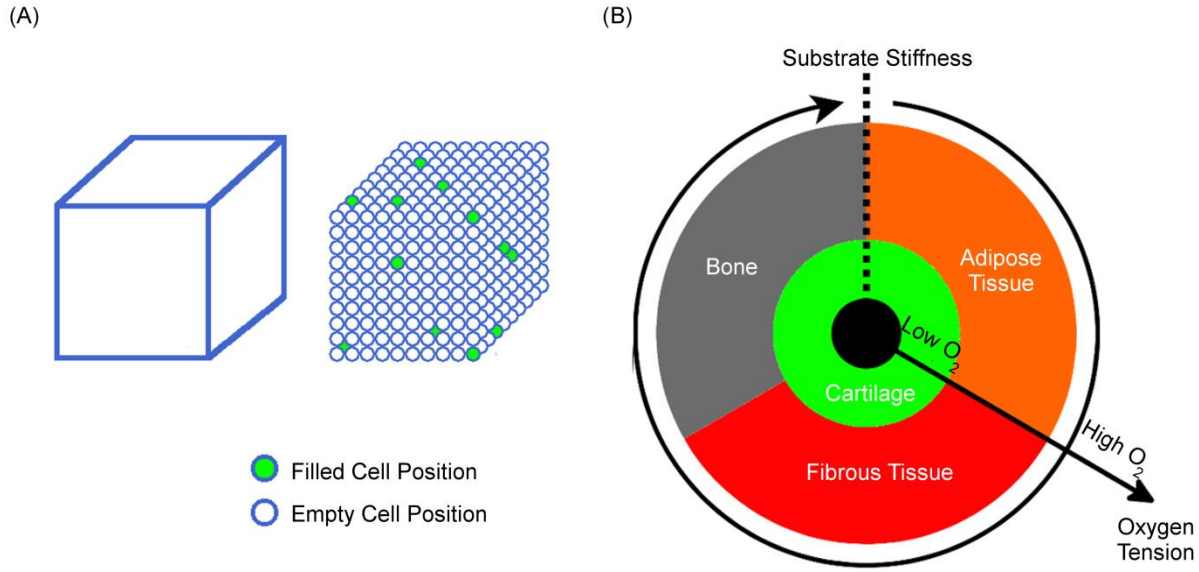


*Figure 3: (A) A 3-dimensional finite element with corresponding lattice. Each lattice point represents a potential location for a cell. (B) Tissue differentiation algorithm as directed by the local oxygen tension and substrate stiffness.*

Endochondral ossification was modelled as a two-step process which first involved CCs becoming hypertrophic before ossification of the tissue began [47]. Based on the literature, it was assumed that the first step occurred in regions where the oxygen tension increased beyond a threshold value ($O_2^{hypertrophic}$) [48–50]. Following this, the second step depicted the ossification process whereby HCs either transdifferentiate into, or are replaced by invading OBs [47,51,52]. In this model, HCs were replaced with OBs provided that: 1) they were in an element where the oxygen tension was greater than a threshold value ($O_2^{endochondral}$) (to mimic the invading blood vessels) and 2) they were in the vicinity of an OB (which ensured that bone could only form in the vicinity of bone).

Finally, once an element had committed to a particular phenotype (either bone, cartilage, or fibrous tissue), any remaining MSCs in that element differentiated along that phenotypic pathway. An element was said to have committed to a particular phenotype if 50 % of the total allowable lattice points within the element contained cells (i.e. there had to be a minimum cell density of $0.5 \times 10^5$ cells/mm$^3$). Following this, the element was said to belong to the particular phenotype which made up the majority of cells within the element.

## 2.7 Role of Strain in Cell Differentiation

The tissue differentiation algorithm was updated to include a rule whereby chondrocyte hypertrophy was inhibited in regions where the local octahedral shear strain exceeded a threshold value ($\varepsilon^{oct,\ shear} > \varepsilon^{hypertrophy}$).

Following the development of this rule, an additional cell phenotype was implemented within the model in order to differentiate between cartilage and mechanically inferior fibrocartilage. In this case MSCs differentiated into fibrochondrocytes (FCs) when the oxygen tension was hypoxic ($O_2 \leq O_2^{hypertrophic}$) and the magnitude of the local octahedral shear strain exceeded a threshold value ($\varepsilon^{oct,\ shear} > \varepsilon^{fibrocartilage}$). It was assumed that, when exposed to these stimuli, CCs transdifferentiated into FCs. Finally FCs acted in the same way as chondrocytes and thus, became hypertrophic when exposed to the appropriate conditions.

## 2.8 Study design

The results from the *in vitro* study conducted by Thorpe *et al.* [17] were used to develop the rule whereby chondrocyte hypertrophy is inhibited above a specific level of octahedral shear strain. To achieve this the model was used to predict chondrocyte hypertrophy within the different construct groups over the 21-day loading period (confined FS, unconfined FS, confined DC and unconfined DC). At the end of each simulation, the model was tested by comparing the predicted spatial arrangement of chondrocyte hypertrophy to histology slides depicting calcific deposition within the respective groups. In this case it was assumed that calcific deposition was indicative of chondrocyte hypertrophy. The simulations of the FS experimental groups were used to further test our previous hypothesis that chondrocyte hypertrophy is regulated by the local oxygen tension. Following this, the DC groups were then modelled to determine the value of the parameter $\varepsilon^{hypertrophy}$, and hence consider the role of mechanics in regulating hypertrophy in our mechanobiological model. To achieve this, a parametric study was conducted where $\varepsilon^{hypertrophy}$ was varied between 5 % and 15 %, and the results of simulations compared to experimental observations

For each model a number of assumptions were made, based on the experimental findings. Firstly, as the authors did not observe a change in the cell number in any of the experimental groups, cell proliferation and cell death were not included in the simulations. It was also assumed that at the start of each simulation the constructs only contained CCs which could eventually undergo hypertrophy. Each simulation was run iteratively where each iteration represented a time period of 24 hours. Finally, based on studies which have shown

that chondrocyte hypertrophy is inhibited by DC [12,17] , the *in vitro* simulations were used to test whether different measurements of strain (e.g. miminum principal strain, hydrostatic strain) could be used to regulate hypertrophy (See Supplementary Material: Section 8.3).

In the second part of the study the updated model was used to predict the course of the spontaneous repair process within an osteochondral defect over a time period of 14 weeks. Similar to the *in vitro* simulations each iteration modelled a time period of 24 hours. Following this the models were used to develop and validate the rule where fibrocartilage forms instead of cartilage if the octahedral shear strain exceeds a threshold value ($\varepsilon^{fibrocartilage}$). In this case the parameter $\varepsilon^{fibrocartilage}$ was varied between 10 %, 12.5 % and 15 % strain. As an additional part of this study, based on reports that dynamic tensile strain is required to promote fibrocartilage formation [18–20], alternative measures of strain were again examined (See Supplementary Material: Section 8.4).

# 3 Results

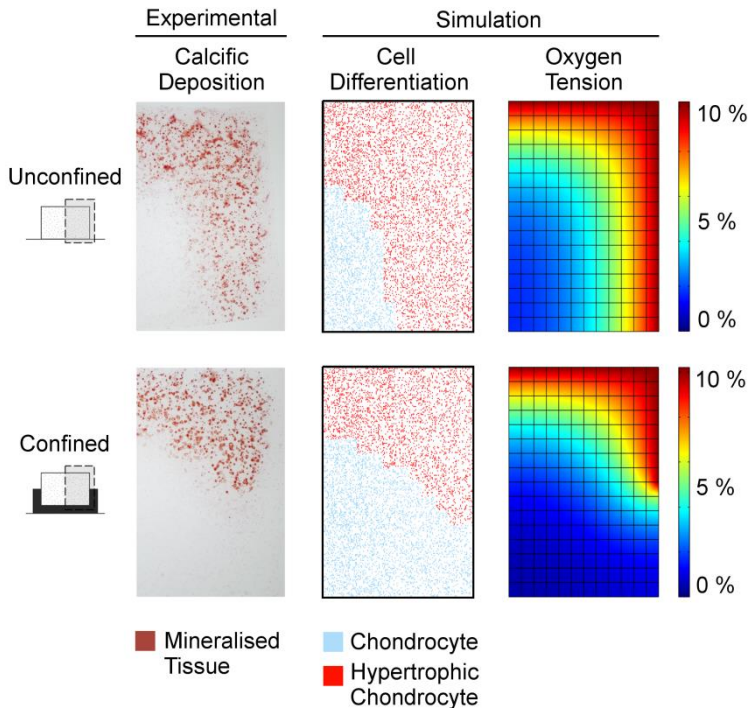


*Figure 4: Experimental and simulation results for the In vitro FS groups. Alcian red staining was used to determine the spatial arrangement of calcific deposition (and chondrocyte hypertrophy) in the unconfined and confined groups following 21 days of FS culture. These were compared to the predicted spatial distribution of chondrocyte hypertrophy and oxygen tension from the unconfined and confined in silico models of the FS groups.*

## 3.1 *Simulation of In Vitro* Models

The tissue differentiation algorithm was able to predict the spatial distribution of chondrocyte hypertrophy (calcification) which was experimentally observed in the confined

and unconfined FS groups (Figure 4). As previously shown, partial confinement of MSC-laden hydrogels was predicted to lower oxygen levels within the bottom of these constructs (Figure 4). In response to these lower levels of oxygen, hypertrophy was predicted to be confined to the exposed surfaces of the MSC-laden hydrogels. In the unconfined group, only the core of the construct did not calcify. These results provide support for the model hypothesis that chondrocyte hypertrophy is regulated by the local oxygen tension.

Following this, the results of the DC experiments were used to develop the rule whereby hypertrophy is inhibited by the local octahedral shear strain. DC resulted in a decrease in hypertrophy and mineralisation. It also resulted, however, in a complex, and irregular spatial distribution of hypertrophic cartilage (Figure 5). In the unconfined DC group, hypertrophy was limited to the top half of the construct, while in the confined group mechanical stimulation nearly completely supressed calcification. The *in silico* models of the unconfined DC group predicted that hypertrophy was completely inhibited when the threshold value $\varepsilon^{hypertrophy}$ was 10 % or less (Figure 5B). Similarly, in the confined DC simulations, as the magnitudes of strain were much higher, hypertrophy was completely inhibited within the construct even if the value of $\varepsilon^{hypertrophy}$ was increased to 30 % (data not shown). Based on these results it was hypothesised that for the *in vivo* simulations, the parameter $\varepsilon^{hypertrophy}$ was within the range of 5 % and 10 % strain.

Additional rules were also tested whereby hypertrophy was inhibited by the third principal strain and by a combination of the octahedral shear strain and the hydrostatic strain (Supplementary Material: Section 8.3). In the case of the third principal strain, the results were similar to those obtained using the octahedral shear strain rule (i.e. for both groups hypertrophy was inhibited below a threshold value) (Supplementary Figure 3). In the simulations for the final rule, where the deformation had to be compressive for hypertrophy to be inhibited ($\varepsilon^{hydrostatic} < 0$), the models were unable to predict the experimental behaviour (hypertrophy was not inhibited by DC) (Supplementary Figure 4). The reason for this was that the FE models predicted that the hydrostatic strain was approximately zero, due to the assumption that the fluid phase was incompressible.

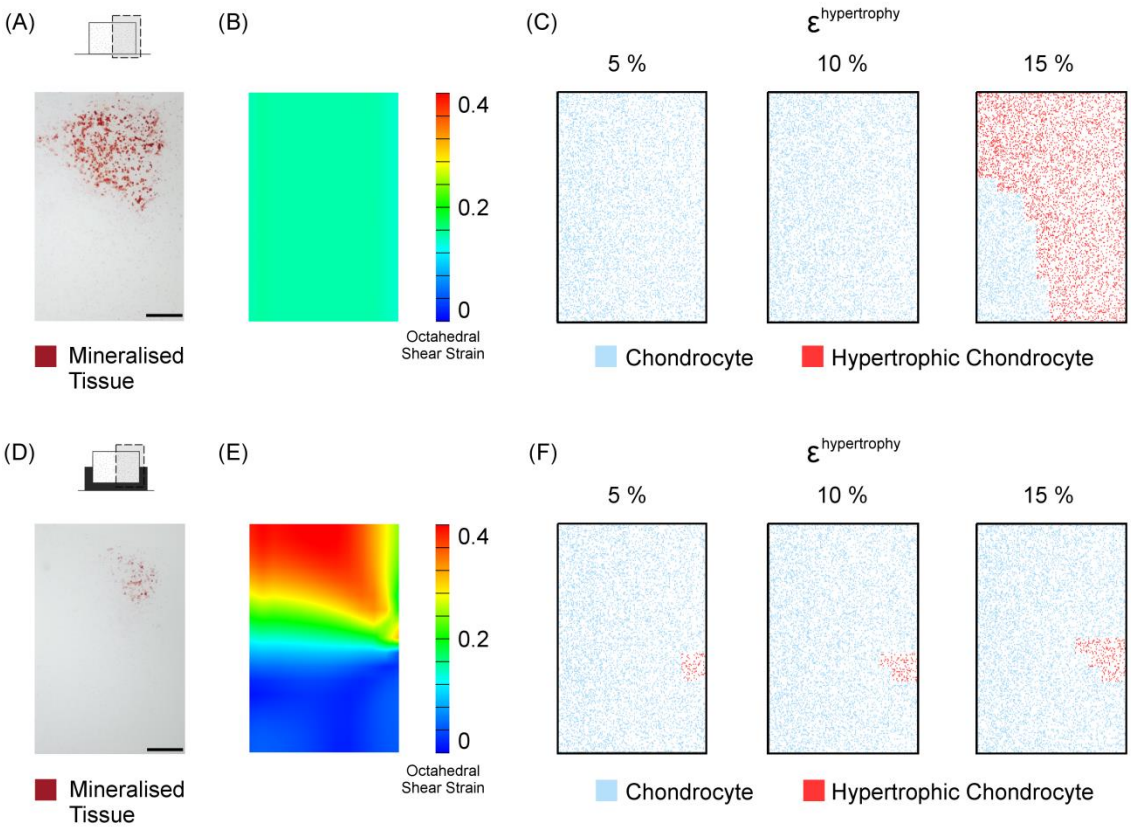


*Figure 5: Experimental and simulation results for the in vitro DC groups where chondrocyte hypertrophy was inhibited by the octahedral shear strain. (A; D) The spatial arrangement of calcific deposition (and chondrocyte hypertrophy) determined for the unconfined and confined groups after 21 days of DC. (B; E) The octahedral shear strain predicted by the unconfined and confined FE models at the day 0 of DC. (C; F) The predicted spatial arrangement of chondrocyte hypertrophy for the unconfined and confined in silico models after 21 days of DC for different values of* $\varepsilon^{hypertrophy}$.

## 3.2 Simulation of spontaneous repair; inhibition of chondrocyte hypertrophy in response to tissue strain

The spontaneous repair process within an osteochondral defect was first simulated using our original computational model which assumed that mechanics indirectly affects tissue formation by regulating angiogenesis (Figure 6A). In the simulation, by week 2, osteogenesis at the exposed cancellous bone was predicted. Due to the limited oxygen supply, however, most of the MSCs in this region differentiated into chondrocytes. At the same time, as a result of the oxygen supplied by the synovial fluid, fibrous tissue was predicted to form above a layer of cartilage at the defect surface. By week 4, as blood vessels penetrated further into the defect, the cartilage in the base became hypertrophic and was converted to bone by endochondral ossification. At this stage, the ossified tissue had formed in a cylindrical shape. By week 8 the advancing bone formed in an infundibuliform (funnel) shape as it approached the chondral region. This infundibuliform shape was retained for the

remainder of the simulation. Finally, by week 18 the majority of the tissue in the defect (> 90 %) was predicted to be bone.

The tissue differentiation algorithm was then updated to include the condition whereby hypertrophy was inhibited in regions of high octahedral shear strain (Figure 6B – D). The threshold value ($\varepsilon^{hypertrophy}$) was set at either 5 %, 7.5 % or 10 %. Up until week 8, all three models predicted the same spatial and temporal pattern of healing as that predicted using the original tissue differentiation algorithm. Beyond this time point, however, the updated model predicted a different pattern of tissue formation. Firstly, as the subchondral plate advanced towards the chondral region, chondrocyte hypertrophy and endochondral ossification were inhibited at the peripheries of the defect as a result of the high strains in this region. In conjunction with this, stress-shielding from the native tissues ensured that the magnitude of the strain in the core of the defect remained low. The result of this was that bone advanced towards the surface through the centre of the defect. This ensured that, from week 12 the advancing bone plate began to become plane with the native subchondral bone. Following this, the bone front was predicted to adopt a convex phase as it advanced into the chondral region of the defect. The main effect that the parameter $\varepsilon^{hypertrophy}$ then had on the model predictions was that it determined the distance that the subchondral plate had advanced by week 18. This distance was smallest for $\varepsilon^{hypertrophy}$ = 5 % (Figure 6B); by week 18 a region of cartilage remained in the chondral phase of the defect when this value was implemented. Conversely, when $\varepsilon^{hypertrophy}$ = 10 % (Figure 6D), very little cartilage was predicted in the defect by this time point.

Similar results were obtained for the simulations where the different measures of strain were used to inhibit hypertrophy. In the case where the 3$^{rd}$ principal strain was used, the spatial pattern of bone first adopted a cylindrical shape, then infundibuliform, then planer and finally, a convex arrangement as the subchondral plate advanced towards the surface of the defect (Supplementary Figure 5B - D). Furthermore, the threshold value ($\varepsilon^{hypertrophy}$) determined the distance that the subchondral plate had advanced by week 18. This behaviour was also observed in the simulations where a combination of the hydrostatic strain and the octahedral strain were used to inhibit hypertrophy (Supplementary Figure 6B – D). In these simulations however, unlike in the models where hypertrophy was inhibited by either the octahedral shear strain or the 3$^{rd}$ principal strain, the advancing bone front adopted a jagged appearance.

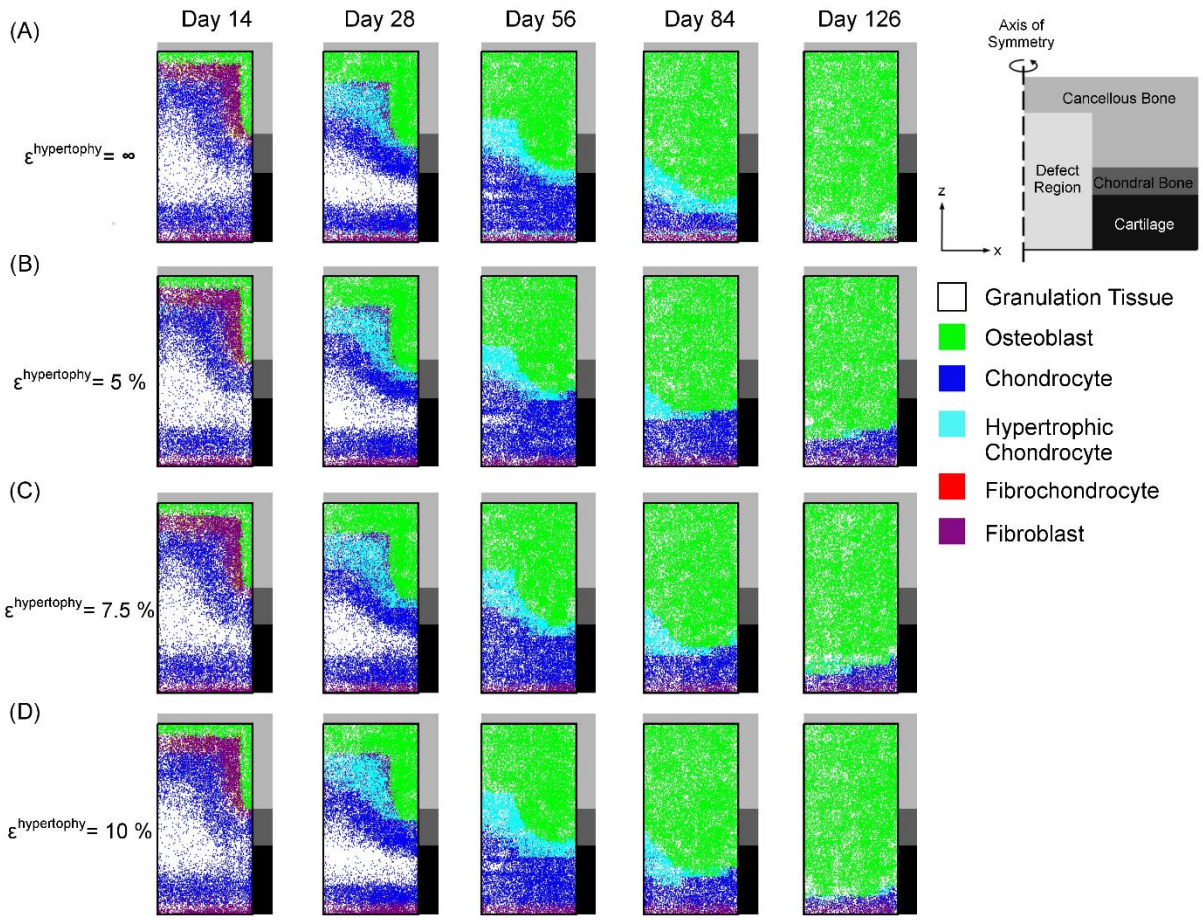


*Figure 6: Model predictions of cell differentiation at different times during the spontaneous repair of an osteochondral defect using: (A) our previous tissue differentiation algorithm where chondrocyte hypertrophy was regulated solely by the oxygen tension (B – D) an updated algorithm where chondrocyte hypertrophy was regulated by the oxygen tension and the octahedral shear strain. The parameter $\varepsilon^{hypertrophy}$ was varied between (B) 5 %, (C) 7.5 % and (D) 10 %:*

## 3.3 Simulation of spontaneous repair; formation of fibrocartilage in response to tissue strain

In the final part of this study the tissue differentiation algorithm was further updated to include the condition whereby fibrocartilage formed, in an otherwise chondrogenic environment, when the octahedral shear strain exceeded a critical value $\varepsilon^{fibrocartilage}$ (Figure 7). The parameter $\varepsilon^{hypertrophy}$ was fixed at 5 %, while the parameter $\varepsilon^{fibrocartilage}$ was set at either 10 %, 12.5 % or 15 %. The value of $\varepsilon^{fibrocartilage}$ had a large effect on the model predictions. In the simulation where $\varepsilon^{fibrocartilage}$ = 10 %, a mixture of fibrous tissue and fibrocartilage formed at the surface of the defect as early as week 2 (Figure 7A). By week 8, as the vascular network was restored to the subchondral region, bone filled the majority of the osseous phase of the defect and hyaline cartilage formed below the fibrocartilage within the chondral phase of the defect. As the simulation progressed, the subchondral plate advanced above the native tidemark and the hyaline cartilage was replaced with bone by endochondral ossification.

Hypertrophy was inhibited within the fibrocartilage, however, as a result of the high strain environment. By week 18 no hyaline cartilage remained in the defect. Instead the chondral phase was composed entirely of osseous tissue covered by a thin layer of fibrocartilage and fibrous tissue.

A different pattern of tissue formation was predicted in the simulation where $\varepsilon^{fibrocartilage}$ = 12.5 % (Figure 7B). In this model, by week 2, a mixture of hyaline cartilage, fibrocartilage and fibrous tissue formed at the surface of the defect. Furthermore, by week 8, the majority of the chondral phase was composed of hyaline cartilage with only a small region of fibrocartilage predicted at the surface of the defect. As the bone plate advanced into the chondral phase, however, the magnitude of the strains within this tissue were amplified and the hyaline cartilage was converted into fibrocartilage. By week 18, the spatial distribution of tissues predicted by the model was the same as that predicted in the simulation where $\varepsilon^{fibrocartilage}$ = 10 %. Finally, in the model where $\varepsilon^{fibrocartilage}$ = 15 %, very little fibrocartilage formed and by week 18, only a small region was predicted at the surface of the defect (Figure 7C).

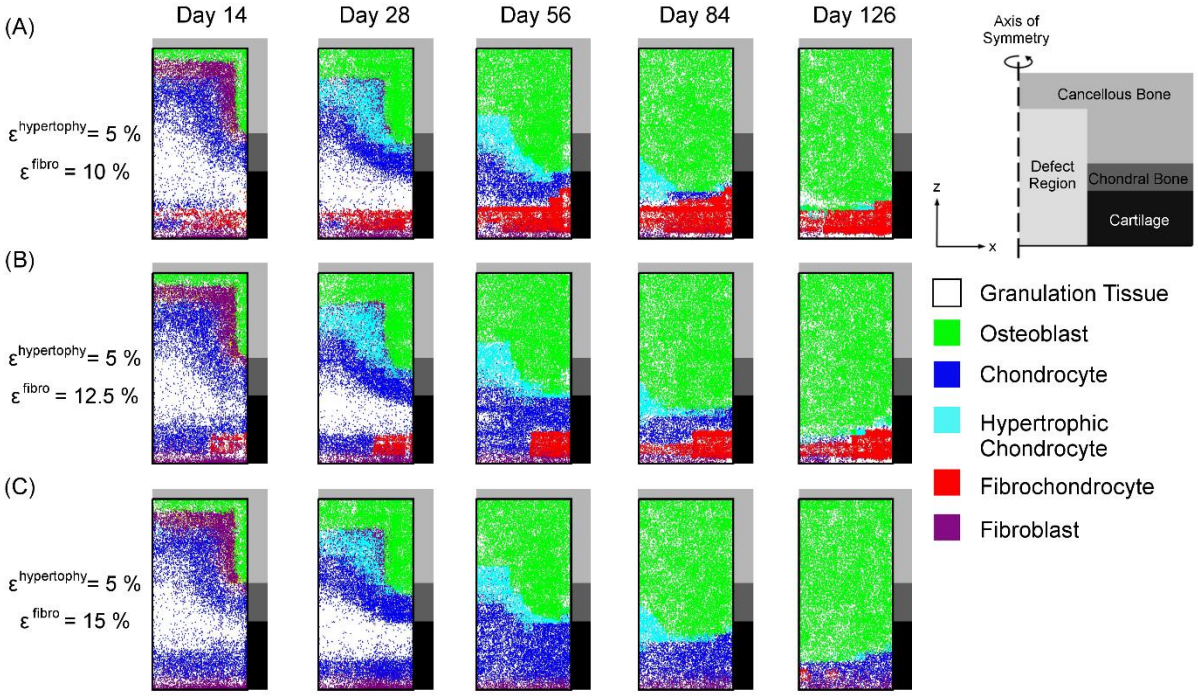


*Figure 7: Model predictions of cell differentiation at different times during the spontaneous repair of an osteochondral defect using the updated algorithm where chondrocyte hypertrophy was regulated by the oxygen tension and the octahedral shear strain ($\varepsilon^{hypertrophy}$= 5 %) and fibrocartilage could form based on the local octahedral shear strain. The parameter $\varepsilon^{fibrocartilage}$ was varied between (E) 10 %, (F) 12.5 % and (G) 15 %.*

Alternative measures of strain were used to regulate the formation of fibrocartilage (section 8.4), in the same way as for the hypertrophy rule. These included the first principal strain (Supplementary Figure 7) and a combination of the hydrostatic strain and the octahedral shear strain (Supplementary Figure 8). Both of these conditions produced similar results to the simulations where fibrocartilage was regulated by the octahedral shear strain. When the threshold value was sufficiently low the majority of fibrocartilage formed prior to week 8. When it was sufficiently high, the majority of fibrocartilage formed after the subchondral plate had advanced beyond the native tissue, and when it was too high no fibrocartilage formed within the defect.

# 4 Discussion

In a previous study we developed a computational mechanobiological model which predicted cell fate during the spontaneous repair process within an osteochondral defect. While this model successfully simulated many aspects of the regenerative process, it was unable to predict the spatial pattern of bone formation observed during the latter stages of repair. The objective of this study was thus to improve the predictive capacity of the model by including a series of rules whereby the local mechanical environment affected the fate of cartilage. Based on the findings of a number of *in vitro* studies which have shown that mechanical loading can either prevent hypertrophy and endochondral ossification of cartilage [12–16], or promote the formation of fibrocartilage [18,19], it was hypothesised that the fate of the cartilage that forms within an osteochondral defect depends on both oxygen availability and the local mechanical environment. It was postulated that hypertrophy was supressed by appropriate magnitudes of local strain, while fibrocartilage formed in regions where the local strain was excessively high. These rules were developed by first modelling the *in vitro* bioreactor study conducted by Thorpe *et al.* [17]. In this study, dynamic compression of agarose hydrogels which were seeded with MSC-derived chondrocytes led to a reduction in chondrocyte hypertrophy and calcification of the engineered tissue. The updated tissue differentiation algorithm was then used to model the spontaneous repair process within an osteochondral defect. The pattern of tissue formation predicted by these simulations matched the behaviour experimentally observed in a number of *in vivo* models. In addition to this, the models also provide insights into how mechanical loading benefits the spontaneous repair process by inhibiting chondrocyte hypertrophy and endochondral ossification during

the latter stages of repair. The models also point to the deleterious effect that loading can have on the process by inducing the formation of fibrocartilage in place of hyaline cartilage.

The first objective in modelling the *in vitro* study conducted by Thorpe *et al.* [17] was to simulate the hypertrophic progression observed within unloaded MSC laden hydrogels, in order to provide additional support for our previous hypothesis that chondrocyte hypertrophy is inhibited by low oxygen availability. In this case, using our original tissue differentiation algorithm, where chondrocyte hypertrophy was regulated solely by the local oxygen tension, the simulations were able to predict the experimentally observed spatial distribution of mineralisation within the confined and unconfined constructs. Following this, the experimental findings that the application of DC supressed mineralization of MSC-laden hydrogels were used to develop the rules whereby chondrocyte hypertrophy is inhibited by the local strain environment. In the developed models chondrocyte hypertrophy was not predicted in either of the DC groups when the threshold parameter, $\varepsilon^{hypertrophy}$, was below a specific value. The model was therefore unable to predict the spatial pattern of hypertrophy observed in the unconfined group. This was most likely caused by the assumption that the constructs contained a homogeneous distribution of extra cellular matrix (ECM) components at the onset of DC. In reality, histological staining performed prior to the DC loading protocol showed that the ECM was distributed in a heterogeneous arrangement (data not shown) [17]. In addition to this, as a result of the high oxygen tension within the top half of the construct, prior to the application of DC, cells within this region may have undergone hypertrophy and begun mineralising their surrounding tissue. These factors may then have resulted in the upper section of the construct being stiffer than the bottom section of the construct at the onset of loading. This strain shielding effect would have reduced the strains in the top half of the construct (where chondrocyte hypertrophy was experimentally observed) and amplified the strains in the bottom half of the construct (where chondrocyte hypertrophy was not observed). Despite these simplifications, however, the developed models were able to predict the general trends observed by Thorpe *et al.*[17] whereby the application of DC led to a reduction in chondrocyte hypertrophy.

In addition to the octahedral shear strain, the third principal strain and the hydrostatic strain were examined as inhibiters of chondrocyte hypertrophy (Supplementary Material: Sections 8.3 and 8.4). In the case of the latter approach, hypertrophy was inhibited in regions where the magnitude of the 3rd principal strain exceeded a threshold value ($\varepsilon^{min} \geq \varepsilon^{hypertrophy}$).

The predicted results from these simulations followed the same trends as the models where the octahedral shear strain was used to inhibit hypertrophy. Conversely, in the case of hydrostatic strain, hypertrophy was inhibited in regions where the deformation was compressive ($\varepsilon^{hydrostatic} < 0$) and appropriately high ($\varepsilon^{oct,shear} \geq \varepsilon^{hypertrophy}$). These simulations were unable to predict the experimentally observed behaviour because the calculated hydrostatic strain was approximately zero in all of the models. This arose due to the assumptions that the fluid phase was incompressible and that the constructs had the same material parameters as native cartilage (i.e. low permeability). Based on these findings, the octahedral shear strain was considered as an appropriate measure of strain for use in the updated tissue differentiation algorithm where tissue strain directly influenced chondrocyte fate.

Following the development of the *in vitro* simulations, the updated tissue differentiation algorithm was then used to model the spontaneous repair process within an osteochondral defect. The purpose of this was, firstly, to determine a value for the parameter $\varepsilon^{hypertrophy}$ and, secondly, to develop an additional rule whereby excessive magnitudes of strain, coupled with chondrogenic conditions, resulted in the formation of fibrocartilage. By performing a series of parametric studies it was determined that the model where $\varepsilon^{hypertrophy}$ = 5 % and $\varepsilon^{fibrocartilage}$ = 12.5 % was most representative of the experimentally observed behaviour (Figure 8). This model was validated by comparing the spatial patterns of bone formation predicted in the simulation with those experimentally observed during the different stages of the spontaneous repair process [5]. In this *in vivo* study it was reported that the osseous tissue first forms in a cylindrical arrangement, then an infundibuliform shape, before becoming plane with the native bone and eventually advancing into the chondral phase in a convex arrangement (Figure 8A). These different arrangements were predicted at various time points within the updated model.

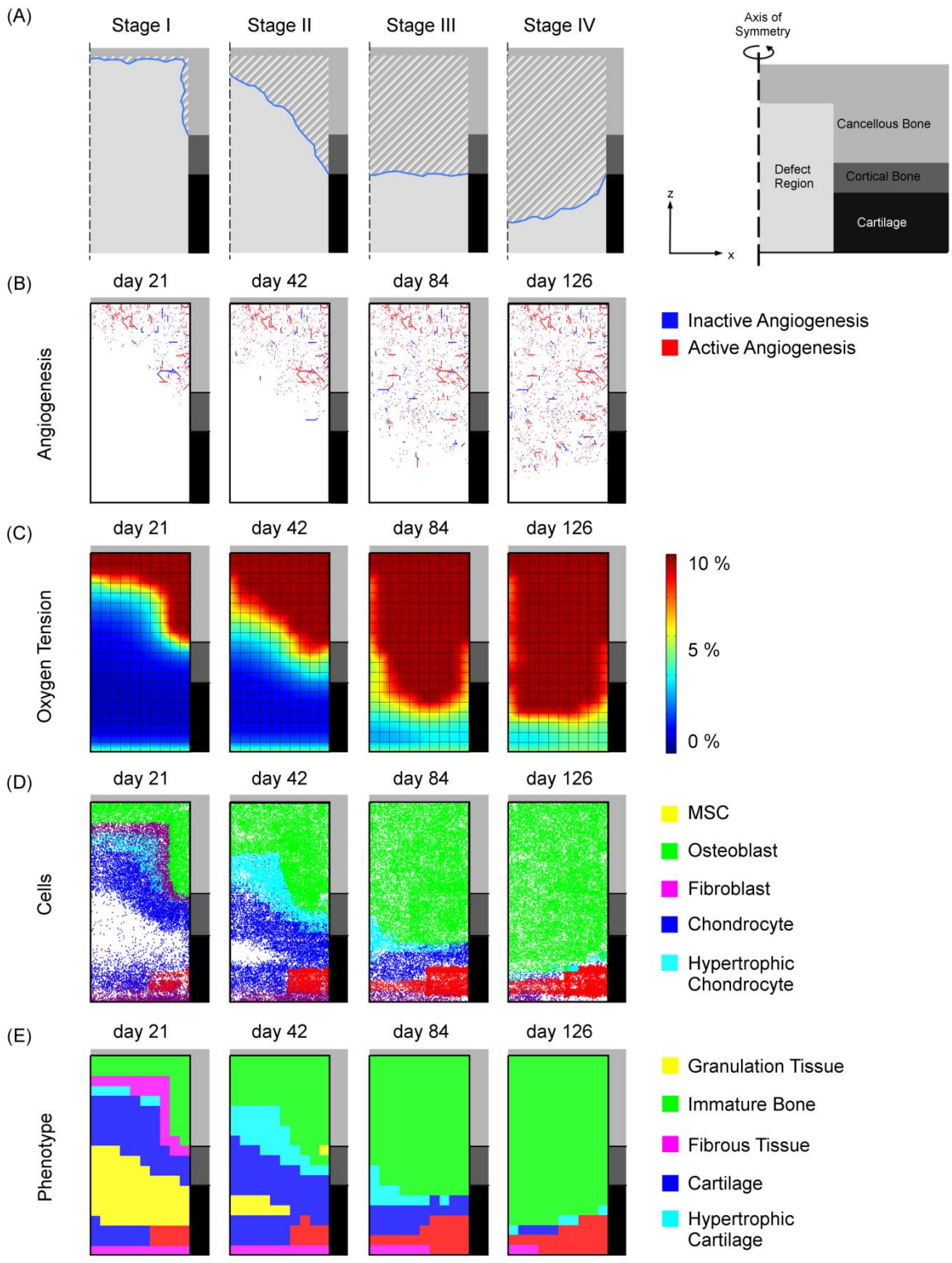


*Figure 8: Model Predictions for the simulations where $\varepsilon^{hypertrophy} = 5$ % and $\varepsilon^{fibrocartilage} = 12.5$ %. (A) The spatial pattern of bone formation within an osteochondral defect observed at different stages of the spontaneous repair process by Orth et al. [5]. (B – D) The model predictions of the spatial pattern of (B) blood vessel growth, (C) oxygen tension, (D) cell differentiation and (E) tissue formation at different stages of the spontaneous repair process within an osteochondral defect.*

The developed model also provides insights into the effect that the changing environment within the osteochondral defect has on the spontaneous repair process. Firstly,

during the initial stages of the repair process (< 8 weeks), as a result of stress shielding from the surrounding tissues, bone formation was controlled largely by oxygen. As the subchondral plate advanced into the chondral phase, however, the mechanical environment began to play a much larger role in directing endochondral ossification, most notably by inhibiting chondrocyte hypertrophy in the peripheries of the defect. These results imply that an appropriate loading regime may improve the treatment of osteochondral defects by inhibiting terminal differentiation and endochondral ossification within the chondral phase. This feature has been explored in a number of *in vivo* studies which have examined the effect that both the magnitude [7,8,11] and the timing of loading [53] has on the outcome of the spontaneous repair process. In all of these studies it was reported that an appropriate loading regime benefited the repair process by promoting the formation of stable hyaline cartilage.

The altering environment also affected the formation of fibrocartilage during the repair process. In the first 8 weeks of the simulation only a small region of fibrocartilage was predicted to form within the chondral phase of the defect. As the subchondral plate advanced above the native tidemark, however, the magnitude of the strains within this phase increased and the remaining hyaline cartilage was converted to fibrocartilage. These results agree with a number of long term *in vivo* studies which have reported that the hyaline cartilage which initially forms in the chondral phase of the defect eventually breaks down [5,54]. It may thus be the case that, the magnitude of the strains within the newly formed chondral tissue increases, as the bone front advances towards the surface of the defect, as observed in the simulations. This may in turn lead to the formation of mechanically inferior fibrocartilage which is unable to withstand the loading environment of the knee joint.

The main limitation of the current study were the FE models which were used to determine the local mechanical environment within the *in vitro* and the *in vivo* cases. These models were simplified by assuming that all of the tissues involved could be characterised as isotropic elastic materials. In reality, however, biological tissues are much more complex and require sophisticated mathematical models to accurately predict their behaviour. As a result of this simplification, it was only possible to predict the general behaviour rather than the exact magnitudes of the strain within the deforming tissue. For this reason, the threshold values $\varepsilon^{hypertrophy}$ and $\varepsilon^{fibrocartilage}$ are exclusive to the models in which they were developed and as a result may change as the model is used to simulate different regenerative events within the *in vivo* setting.

A final simplification which may limit the predictive capacity of the developed model arises in relation to the algorithm which was used to predict angiogenesis within the defect. As part of this study, our previous model of angiogenesis was updated to include a feature whereby blood vessels had to form a closed loop before they were considered active [32]. The benefit of this updated algorithm was that it made the model more physiologically relevant. Despite this feature however, angiogenesis was still considered to be governed largely by the mechanical environment and the contribution of growth factors was, therefore not considered. Studies have shown that during regenerative events there exists a 'cross-talk' between the differentiating cells and the forming blood vessels which may affect tissue formation [55–58]. Such a relationship has been explored as a potential mechanism which may be used to direct the course of endochondral ossification during the repair of osteochondral defects in a number of tissue engineering studies [59–61]. Future work will involve updating the current model to include this behaviour in order to better understand the mechanisms involved in such approaches.

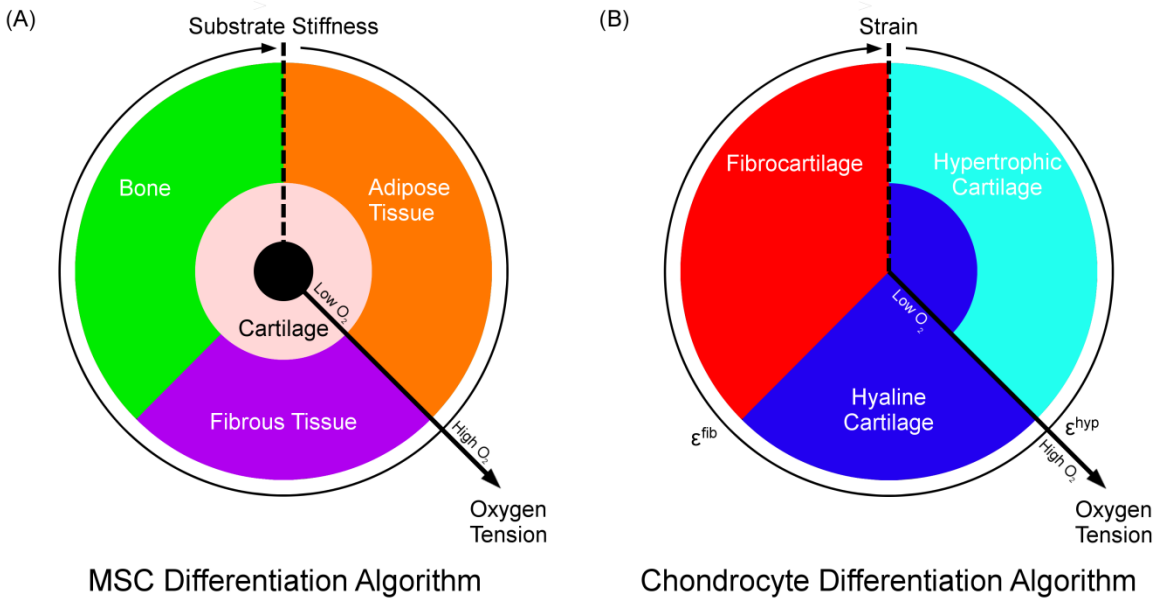


*Figure 9: Updated tissue differentiation algorithm where (A) MSC fate is governed by a combination of the substrate stiffness and local oxygen tension and (B) chondrocyte fate is governed by the octahedral shear strain and the local oxygen tension.*

Despite these limitations, the developed model was able to predict the pattern of tissue formation which has been experimentally observed during the spontaneous repair process within an osteochondral defect. Based on these results we propose an updated version of the tissue differentiation algorithm developed by Burke *et al.*[21] where MSC fate is governed by

the substrate stiffness and the local oxygen tension while the chondrogenic phenotype is affected by the magnitude of the local octahedral shear strain and the local oxygen tension (Figure 9). This model is able to account for the role that mechanical loading plays on the quality of the repair tissue. In particular, the model provides insights into how an appropriate loading regime can improve the repair process by promoting the formation of stable hyaline cartilage. Future work will involve using the developed model to better understand the mechanisms involved in successful and unsuccessful tissue engineering strategies designed to treat osteochondral defect.

# 5 References


1. Gotterbarm, T., Breusch, S. J., Schneider, U. & Jung, M. The minipig model for experimental chondral and osteochondral defect repair in tissue engineering: retrospective analysis of 180 defects. *Lab. Anim.* **42,** 71–82 (2008).

2. Shapiro, F., Koide, S. & Glimcher, M. J. Cell Origin and Differentiation in the Repair of Full-Thickness Defects of Articular Cartilage. *J. Bone Jt. Surg.* **75-A,** 532–53 (1993).

3. Nukavarapu, S. P. & Dorcemus, D. L. Osteochondral tissue engineering: current strategies and challenges. *Biotechnol. Adv.* **31,** 706–21 (2013).

4. Panseri, S. *et al.* Osteochondral tissue engineering approaches for articular cartilage and subchondral bone regeneration. *Knee Surg. Sports Traumatol. Arthrosc.* **20,** 1182–91 (2012).

5. Orth, P. *et al.* Temporal and spatial migration pattern of the subchondral bone plate in a rabbit osteochondral defect model. *Osteoarthr. Cartil.* **20,** 1161–1169 (2012).

6. DePalma, A. F., McKeever, C. D. & Subin, D. K. Process of Repair of Articular Cartilage Demonstrated by Histology and Autoradiography with Tritiated Thymidine. *Clin. Orthop. Relat. Res.* **48,** 229–42 (1966).

7. Salter, R. B. *et al.* The Biological Effect of Continuous Passive Motion on the Healing of Full-Thickness Defects in Articular Cartilage. An Experimental Investigation. *J. Bone Jt. Surg.* **62,** 1232–1251 (1980).

8. Kim, H. K., Moran, M. E. & Salter, R. B. The potential for regeneration of articular cartilage in defects created by chondral shaving and subchondral abrasion. An experimental investigation in rabbits. *J. Bone Jt. Surg.* **73,** 1301–1315 (1991).

9. Chang, N. J. *et al.* The combined effects of continuous passive motion treatment and acellular PLGA implants on osteochondral regeneration in the rabbit. *Biomaterials* **33,** 3153–3163 (2012).

10. Arakaki, K. *et al.* Joint immobilization inhibits spontaneous hyaline cartilage regeneration induced by a novel double-network gel implantation. *J. Mater. Sci. Mater. Med.* **22,** 417–425 (2011).

11. O'Driscoll, S. W., Keeley, F. W. & Salter, R. B. The chondrogenic potential of free autogenous periosteal grafts for biological resurfacing of major full-thickness defects in joint surfaces under the influence of continous passive motion. *J. Bone Jt. Surg.* **68,** 1017–35 (1986).

12. Bian, L., Zhai, D. Y., Zhang, E. C., Mauck, R. L. & Burdick, J. a. Dynamic Compressive Loading Enhances Cartilage Matrix Synthesis and Distribution and Suppresses Hypertrophy in hMSC-

Laden Hyaluronic Acid Hydrogels. *Tissue Eng. Part A* **18,** 715–724 (2012).

13. Thorpe, S. D., Buckley, C. T., Steward, A. J. & Kelly, D. J. European Society of Biomechanics S.M. Perren Award 2012: The external mechanical environment can override the influence of local substrate in determining stem cell fate. *J. Biomech.* **45,** 2483–2492 (2012).

14. Huang, A. H., Farrell, M. J., Kim, M. & Mauck, R. L. LONG-TERM DYNAMIC LOADING IMPROVES THE MECHANICAL PROPERTIES OF CHONDROGENIC MESENCHYMAL STEM CELL-LADEN HYDROGELS. *Eur. Cells Mater.* **19,** 72 – 85 (2010).

15. Mauck, R. L., Byers, B. a., Yuan, X. & Tuan, R. S. Regulation of cartilaginous ECM gene transcription by chondrocytes and MSCs in 3D culture in response to dynamic loading. *Biomech. Model. Mechanobiol.* **6,** 113–125 (2007).

16. Kisiday, J. D., Frisbie, D. D., McIlwraith, C. W. & Grodzinsky, A. J. Dynamic compression stimulates proteoglycan synthesis by mesenchymal stem cells in the absence of chondrogenic cytokines. *Tissue Eng. Part A* **15,** 2817–2824 (2009).

17. Thorpe, S. D., Nagel, T., Carroll, S. F. & Kelly, D. J. Modulating Gradients in Regulatory Signals within Mesenchymal Stem Cell Seeded Hydrogels: A Novel Strategy to Engineer Zonal Articular Cartilage. *PLoS One* **8,** e60764 (2013).

18. Thomopoulos, S. *et al.* Fibrocartilage tissue engineering: the role of the stress environment on cell morphology and matrix expression. *Tissue Eng. Part A* **17,** 1039–1053 (2011).

19. Connelly, J. T., Vanderploeg, E. J., Mouw, J. K., Wilson, C. G. & Levenston, M. E. Tensile loading modulates bone marrow stromal cell differentiation and the development of engineered fibrocartilage constructs. *Tissue Eng. Part A* **16,** 1913–1923 (2010).

20. Baker, B. M., Shah, R. P., Huang, A. H. & Mauck, R. L. Dynamic tensile loading improves the functional properties of mesenchymal stem cell-laden nanofiber-based fibrocartilage. *Tissue Eng. Part A* **17,** 1445–1455 (2011).

21. Burke, D. P. & Kelly, D. J. Substrate stiffness and oxygen as regulators of stem cell differentiation during skeletal tissue regeneration: a mechanobiological model. *PLoS One* **7,** e40737 (2012).

22. Lacroix, D. & Prendergast, P. J. A mechano-regulation model for tissue differentiation during fracture healing: analysis of gap size and loading. *J. Biomech.* **35,** 1163–71 (2002).

23. Hori, R. Y. & Lewis, J. L. Mechanical properties of the fibrous tissue found at the bone-cement interface following total joint replacement. *J. Biomed. Mater. Res.* **16,** 911–27 (1982).

24. Claes, L. E. *et al.* Effects of mechanical factors on the fracture healing process. *Clin. Orthop. Relat. Res.* S132–47 (1998). at <http://www.ncbi.nlm.nih.gov/pubmed/9917634>

25. Ochoa, J. A. & Hillberry, B. M. Permeability of bovine cancellous bone. *Trans. 38th ORS 162* (1992).

26. Wilson, W., Van Rietbergen, B., Van Donkelaar, C. C. & Huiskes, R. Pathways of load-induced cartilage damage causing cartilage degeneration in the knee after meniscectomy. *J. Biomech.* **36,** 845–851 (2003).

27. Kelly, D. J. & Prendergast, P. J. Mechano-regulation of stem cell differentiation and tissue regeneration in osteochondral defects. *J. Biomech.* **38,** 1413–22 (2005).

28. Vaziri, A., Nayeb-Hashemi, H., Singh, A. & Tafti, B. a. Influence of meniscectomy and meniscus replacement on the stress distribution in human knee joint. *Ann. Biomed. Eng.* **36,** 1335–1344 (2008).

29. Yao, J., Salo, A. D., Barbau-McInnis, M. & Lerner, A. L. Finite Element Modeling of Knee Joint Contact Pressures and Comparison to Magnetic Resonance Imaging of the Loaded Knee. in *ASME International Mechanical Engineering Congress and Exposition* (2003).

30. Shirazi, R. & Shirazi-Adl, a. Computational biomechanics of articular cartilage of human knee joint: Effect of osteochondral defects. *J. Biomech.* **42,** 2458–2465 (2009).

31. Checa, S. & Prendergast, P. J. A mechanobiological model for tissue differentiation that includes angiogenesis: a lattice-based modeling approach. *Ann. Biomed. Eng.* **37,** 129–45 (2009).

32. Carlier, A., Geris, L., Gastel, N. Van, Carmeliet, G. & Oosterwyck, H. Van. Oxygen as a critical determinant of bone fracture healing — A multiscale model. *J. Theor. Biol.* **365,** 247–264 (2015).

33. Burke, D. P. & Kelly, D. J. A mechanobiological model of endothelial cell migration and proliferation. *Comput. Methods Biomech. Biomed. Engin.* (2014).

34. Matsumoto, T. *et al.* Mechanical strain regulates endothelial cell patterning in-vitro. *Tissue Eng.* **13,** 207–217 (2007).

35. Hershey, D. & Karhan, T. Diffusion Coefficients for Oxygen Transport in Whole Blood. *AIChE* **14,** 969–972 (1968).

36. Epari, D. R., Lienau, J., Schell, H., Witt, F. & Duda, G. N. Pressure, oxygen tension and temperature in the periosteal callus during bone healing--an in vivo study in sheep. *Bone* **43,**

734–9 (2008).

37. Holzwarth, C. *et al.* Low physiologic oxygen tensions reduce proliferation and differentiation of human multipotent mesenchymal stromal cells. *BMC Cell Biol.* **11,** (2010).

38. Pérez, M. a & Prendergast, P. J. Random-walk models of cell dispersal included in mechanobiological simulations of tissue differentiation. *J. Biomech.* **40,** 2244–53 (2007).

39. Sengers, B. G., van Donkelaar, C. C., Oomens, C. W. J. & Baaijens, F. P. T. Computational study of culture conditions and nutrient supply in cartilage tissue engineering. *Biotechnol. Prog.* **21,** 1252–61 (2005).

40. Heywood, H. K., Knight, M. M. & Lee, D. a. Both superficial and deep zone articular chondrocyte subpopulations exhibit the Crabtree effect but have different basal oxygen consumption rates. *J. Cell. Physiol.* **223,** 630–9 (2010).

41. Zhou, S., Cui, Z. & Urban, J. P. G. Factors influencing the oxygen concentration gradient from the synovial surface of articular cartilage to the cartilage-bone interface: a modeling study. *Arthritis Rheum.* **50,** 3915–24 (2004).

42. Lund-Olesen, K. Oxygen tension in synovial fluids. *Arthritis Rheum.* **13,** 769–776 (1970).

43. Isaksson, H., van Donkelaar, C. C., Huiskes, R. & Ito, K. A mechano-regulatory bone-healing model incorporating cell-phenotype specific activity. *J. Theor. Biol.* **252,** 230–46 (2008).

44. Burke, D. *et al.* The role of oxygen as a regulator of stem cell fate during fracture repair in TSP2-null mice. *J. Orthop. Res.* **31,** 1585–96 (2013).

45. Appeddu, P. A. & Shur, B. D. Molecular analysis of cell surface fi-1 , 4-galactosyltransferase function during cell migration. *Proc. Natl. Acad. Sci. U. S. A.* **91,** 2095–2099 (1994).

46. Malda, J. *et al.* Oxygen gradients in tissue-engineered PEGT/PBT cartilaginous constructs: measurement and modeling. *Biotechnol. Bioeng.* **86,** 9–18 (2004).

47. Mackie, E. J., Ahmed, Y. a, Tatarczuch, L., Chen, K.-S. & Mirams, M. Endochondral ossification: how cartilage is converted into bone in the developing skeleton. *Int. J. Biochem. Cell Biol.* **40,** 46–62 (2008).

48. Sheehy, E. J., Buckley, C. T. & Kelly, D. J. Oxygen tension regulates the osteogenic, chondrogenic and endochondral phenotype of bone marrow derived mesenchymal stem cells. *Biochem. Biophys. Res. Commun.* **417,** 305–10 (2012).

49. Ma, T., Grayson, W. L., Frohlich, M. & Vunjak-Novakovic, G. Hypoxia and Stem Cell-Based Engineering of Mesenchymal Tissues. *Biotechnol. Prog.* **25,** 32–42 (2009).

50. Leijten, J. *et al.* Metabolic programming of mesenchymal stromal cells by oxygen tension directs chondrogenic cell fate. *Proc. Natl. Acad. Sci. U. S. A.* (2014). doi:10.1073/pnas.1410977111

51. Yang, G. *et al.* Osteogenic fate of hypertrophic chondrocytes. *Cell Res.* 1–4 (2014). doi:10.1038/cr.2014.111

52. Bahney, C. *et al.* Transdifferentiation of hypertrophic chondrocytes during endochondral bone repair by activation of pluripotent stem cell programs (216.1). *J. Fed. Am. Soc. Exp. Biol.* **28,** (2014).

53. Song, J. Q. *et al.* Effect of treadmill exercise timing on repair of full-thickness defects of articular cartilage by bone-derived mesenchymal stem cells: An experimental investigation in rats. *PLoS One* **9,** 1–10 (2014).

54. Qui, Y. S., Shahgaldi, B. F., Revell, W. J. & Heatley, F. W. Observations of subchondral plate advancement during osteochondral repair: A histomorphometric and mechanical study in the rabbit femoral condyle. *Osteoarthr. Cartil.* **11,** 810–820 (2003).

55. Orth, P., Cucchiarini, M., Kohn, D. & Madry, H. Alterations of the subchondral bone in osteochondral repair--translational data and clinical evidence. *Eur. Cell. Mater.* **25,** 299–316; discussion 314–6 (2013).

56. Gerber, H.-P. *et al.* VEGF couples hypertrophic cartilage remodeling , ossification and angiogenesis during endochondral bone formation. *Nat. Med.* **5,** 623–628 (1999).

57. Gerber, H. P. & Ferrara, N. Angiogenesis and bone growth. *Trends Cardiovasc. Med.* **10,** 223–228 (2000).

58. Sakata, R. *et al.* Localization of vascular endothelial growth factor during the early stages of osteochondral regeneration using a bioabsorbable synthetic polymer scaffold. *J. Orthop. Res.* **30,** 252–259 (2012).

59. Hunziker, E. B. Articular cartilage repair: basic science and clinical progress. A review of the current status and prospects. *Osteoarthritis Cartilage* **10,** 432–63 (2002).

60. Hunziker, E. B. & Driesang, I. M. K. Functional barrier principle for growth-factor-based articular cartilage repair. *Osteoarthr. Cartil.* **11,** 320–327 (2003).

61. Nagai, T. *et al.* Intravenous administration of anti-vascular endothelial growth factor

humanized monoclonal antibody bevacizumab improves articular cartilage repair. *Arthritis Res. Ther.* **12,** R178 (2010).

62. Bian, L., Mauck, R. L. & Burdick, J. a. Dynamic Compressive Loading and Crosslinking Density Influence the. in *Proceedings of the ASME 2012 Summer Bioengineering Conference.* 23–24 (2012).

# 6 List of Tables

# 7 List of Figures

# 8 Supplementary Material

## 8.1 Iterative Model

Tissue differentiation within the osteochondral defect was simulated via an iterative procedure similar to the one outlined by Burke et al. [21] (**Error! Reference source not found.**). Briefly, a finite element model was used to predict the strain environment within the defect. The results of this were then used an inputs to a model of angiogenesis which was run in conjunction with models of cell migration, proliferation and death. Both the angiogenesis and cell models then provided inputs to an oxygen diffusion model which determined the oxygen environment within the defect. In this case the angiogenesis model was used to update the oxygen boundary condition while the cell model was used to update the oxygen consumption terms. Following this, cell differentiation was simulated, based on the results of the oxygen and cell models. Using the tissue differentiation algorithm, the phenotype of each element was calculated. Finally, the results of this were used to update the material parameters of each element of the FE model before the next iteration was run.

## 8.2 Comparison of Angiogenesis Models

The extent of the effect that implementing the updated model of angiogenesis had on the predicted course of cell differentiation was examined by comparing the results obtained using our original model of blood vessel growth (as outlined in our earlier study) and the updated model (as outlined by Carlier *et al.*). In the original model, all vessels were considered active while in the updated model, vessels only became active once they had formed a closed loop. Both models predicted that blood vessels had penetrated the same distance within the defect at Days 14, 28, 56, 84 and 126. Despite this, in the updated model, as vessels penetrated further into the chondral phase the number of active vessels began to decrease as the rate of vessel fusion exceeded the rate of vessel branching. The result of this was that, although both models predicted the same pattern of stem cell differentiation up until day 56, beyond this time point the spatial distribution of the cellular phenotypes began to differ between the two models. By day 84 the original model had predicted that all of the remaining

cartilage had become hypertrophic while in the updated model a region of cartilage remained above the advancing hypertrophic cartilage. Finally, by day 126, the original model had predicted that the entire defect had become bone while in the updated model a small region of fibrous tissue (< 5 % defect volume) remained at the surface of the defect.

Overall, implementing the fusion model of angiogenesis had a small effect on the predicted course of tissue formation during the spontaneous repair process. Despite this, the fusion model was more physiologically relevant, as it ensured that the advancing bone was preceded by a thin region of hypertrophic cartilage. In contrast to this, in the original model, the preceding front of hypertrophic cartilage was much thicker and resulted in the entire chondral phase becoming hypertrophic prior to the advancement of the subchondral plate beyond the native bone.

## 8.3 Alternative Rules for Strain Regulation of Hypertrophy

Alternative rules for the strain regulation of hypertrophy were examined based on the results of *in vitro* studies which have reported that dynamic compressive loading inhibits chondrocyte hypertrophy [17,62]. In the first of these, hypertrophy was inhibited in regions where the local third principal strain was less than a threshold value ($\varepsilon^{min} < \varepsilon^{hypertrophy}$) (Note: the third principal strain is negative and therefore had to be less than the threshold value). The second rule which was examined was that hypertrophy was inhibited in regions where the hydrostatic strain was negative ($\varepsilon^{hydrostatic} < 0$) and the octahedral shear strain exceeded a threshold value ($\varepsilon^{octahedral} > \varepsilon^{hypertrophy}$).

*These rules were tested by using them to model both the in vitro and in vivo behaviours (Supplementary Figure 3, Supplementary Figure 4,*

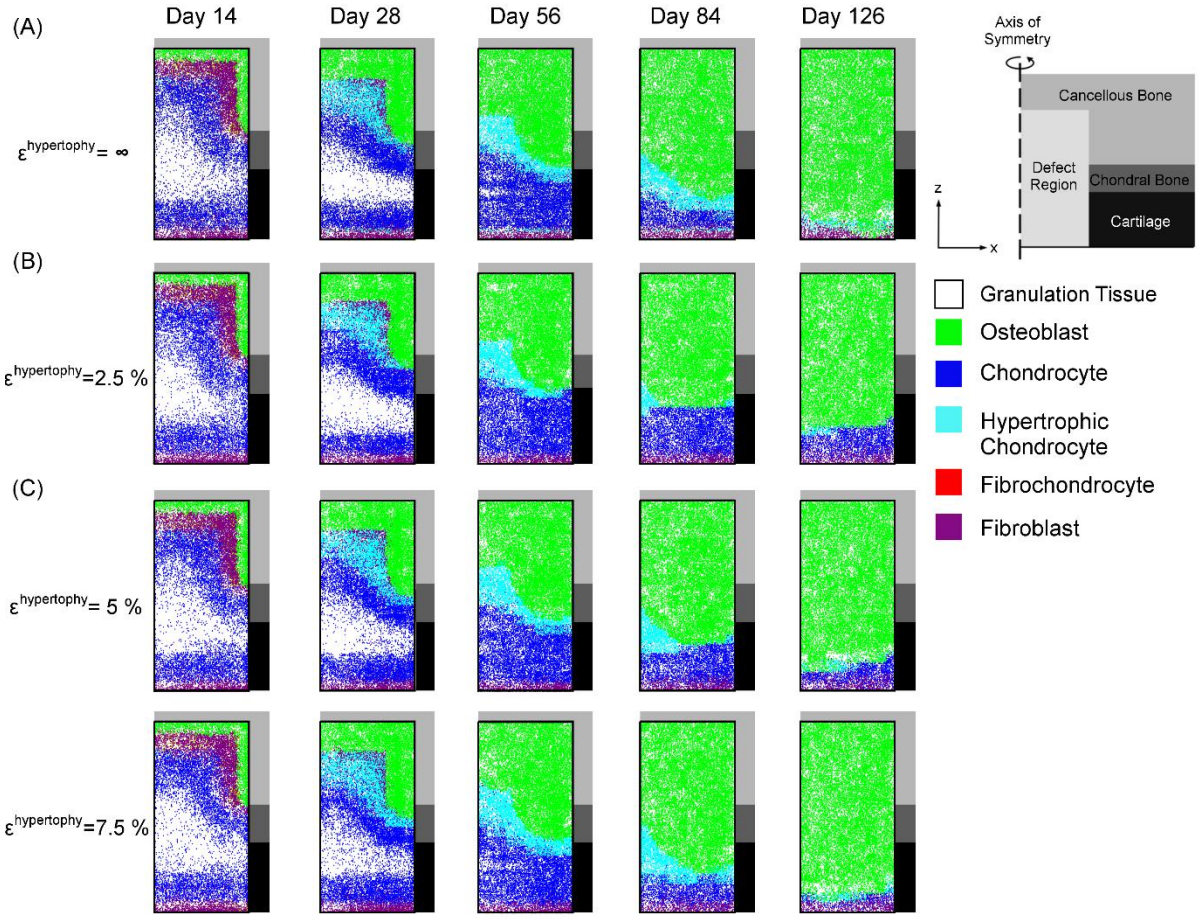


Supplementary Figure 5B - D and Supplementary Figure 6B - D). For the *in vitro* models the value of third principal strain threshold ($\varepsilon^{hypertrophy}$) was varied between -5 %, -10 % and -15 %. For the *in vivo* models these values were varied between -2.5 %, -5 % and -7.5 %. For the hydrostatic strain rule, in the *in vitro* model the threshold value ($\varepsilon^{hypertrophy}$) was varied between 5 %, 10 % and 15 % while for the *in vivo* model this was varied between 5 %, 7.5 % and 10 %.

## 8.4 Alternative Rules for Strain Regulation of Fibrocartilage

Alternative rules for the strain regulation of fibrocartilage were examined based on *in vitro* studies which reported that dynamic tensile loading was required to promote the formation of fibrocartilage. In the first of these, fibrocartilage formed in regions where the local first principal strain exceeded a threshold value ($\varepsilon^{max} > \varepsilon^{fibrocartilage}$). The second rule which was examined was that fibrocartilage formed when the hydrostatic strain was positive

($\varepsilon^{hydrostatic} > 0$) and the octahedral shear strain exceeded a threshold value ($\varepsilon^{octahedral} > \varepsilon^{fibrocartilage}$).

*These rules were tested by using them to model both the spontaneous repair process within an osteochondral defect ( within an osteochondral defect (*

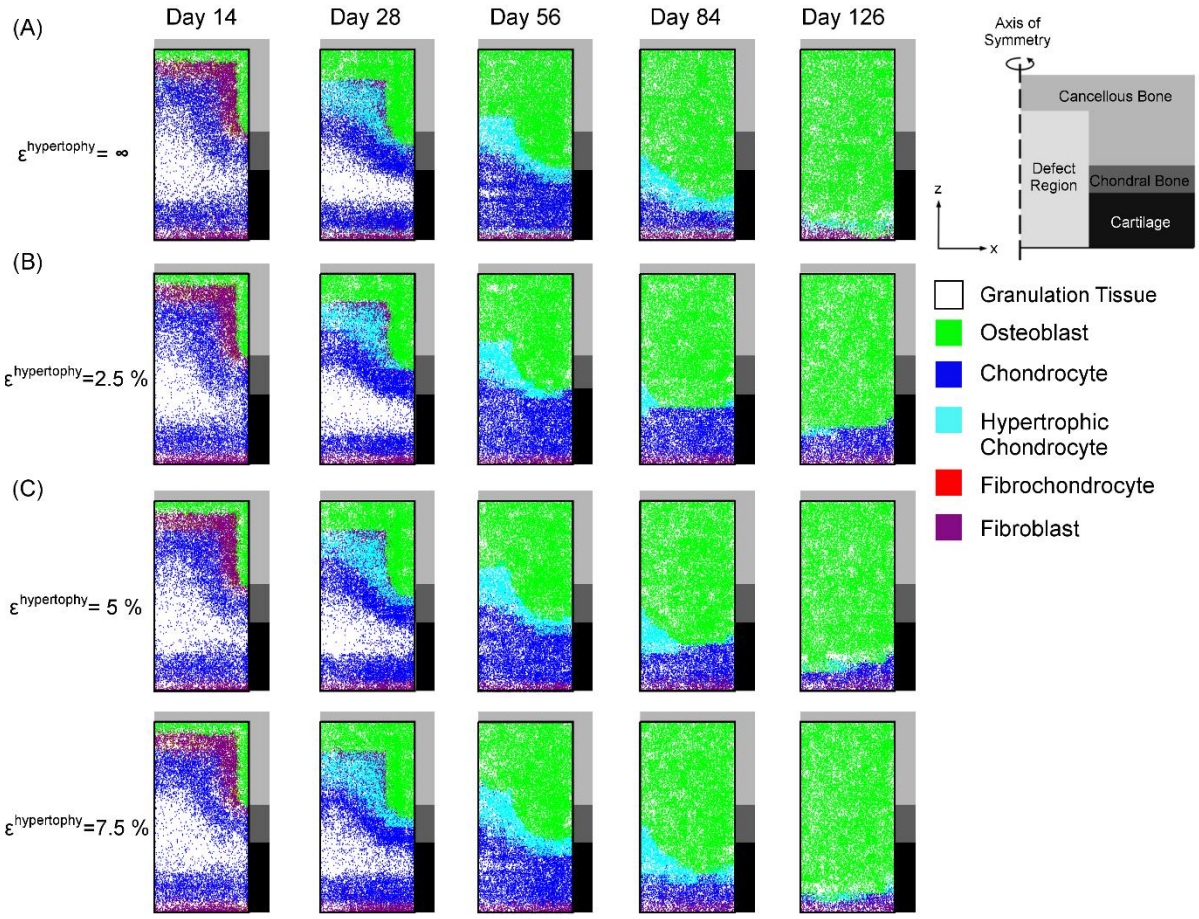


Supplementary Figure 5E - G and Supplementary Figure 6E - G). The value of first principal strain threshold ($\varepsilon^{hypertrophy}$) was varied between 2.5 %, 5 % and 7.5 % while for the hydrostatic strain rule, the threshold value ($\varepsilon^{hypertrophy}$) was varied between 5 %, 7.5 % and 10 %.

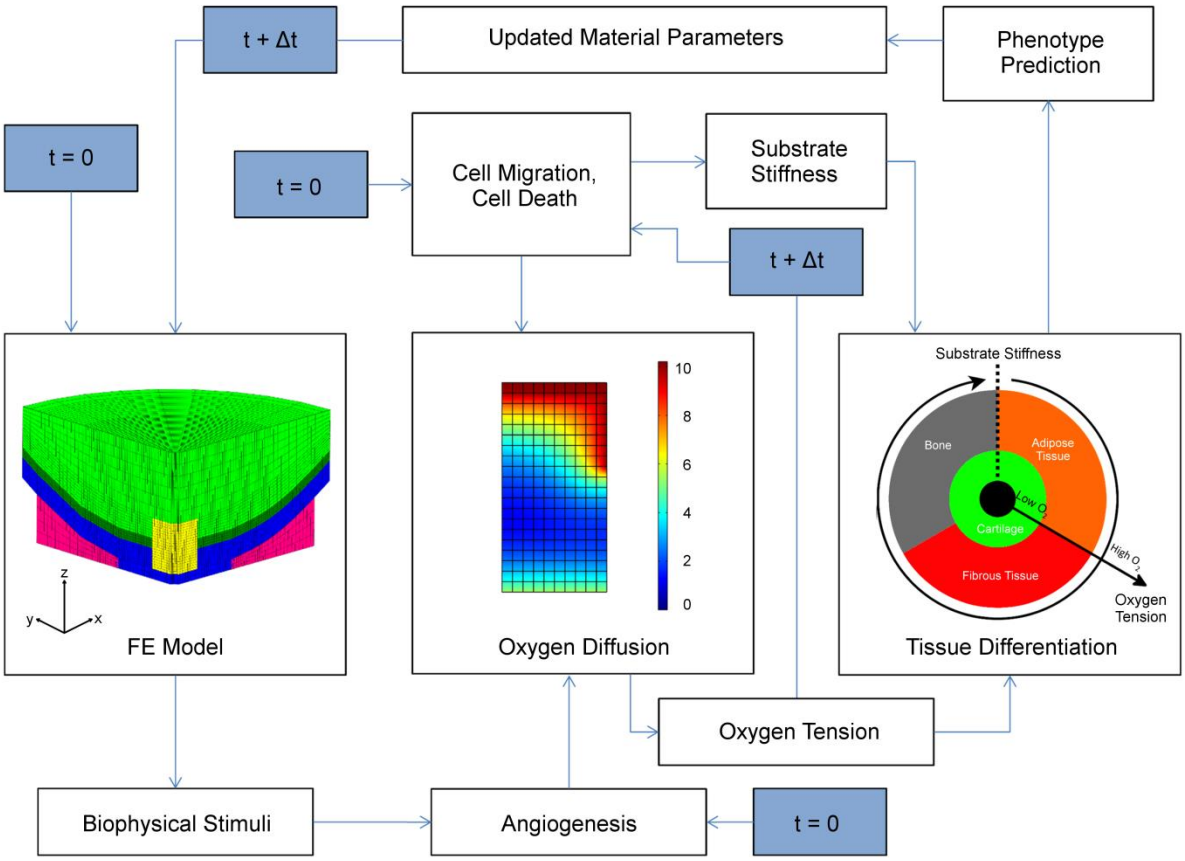


*Supplementary Figure 1: Iterative procedure for the model of the spontaneous repair process within an osteochondral defect.*

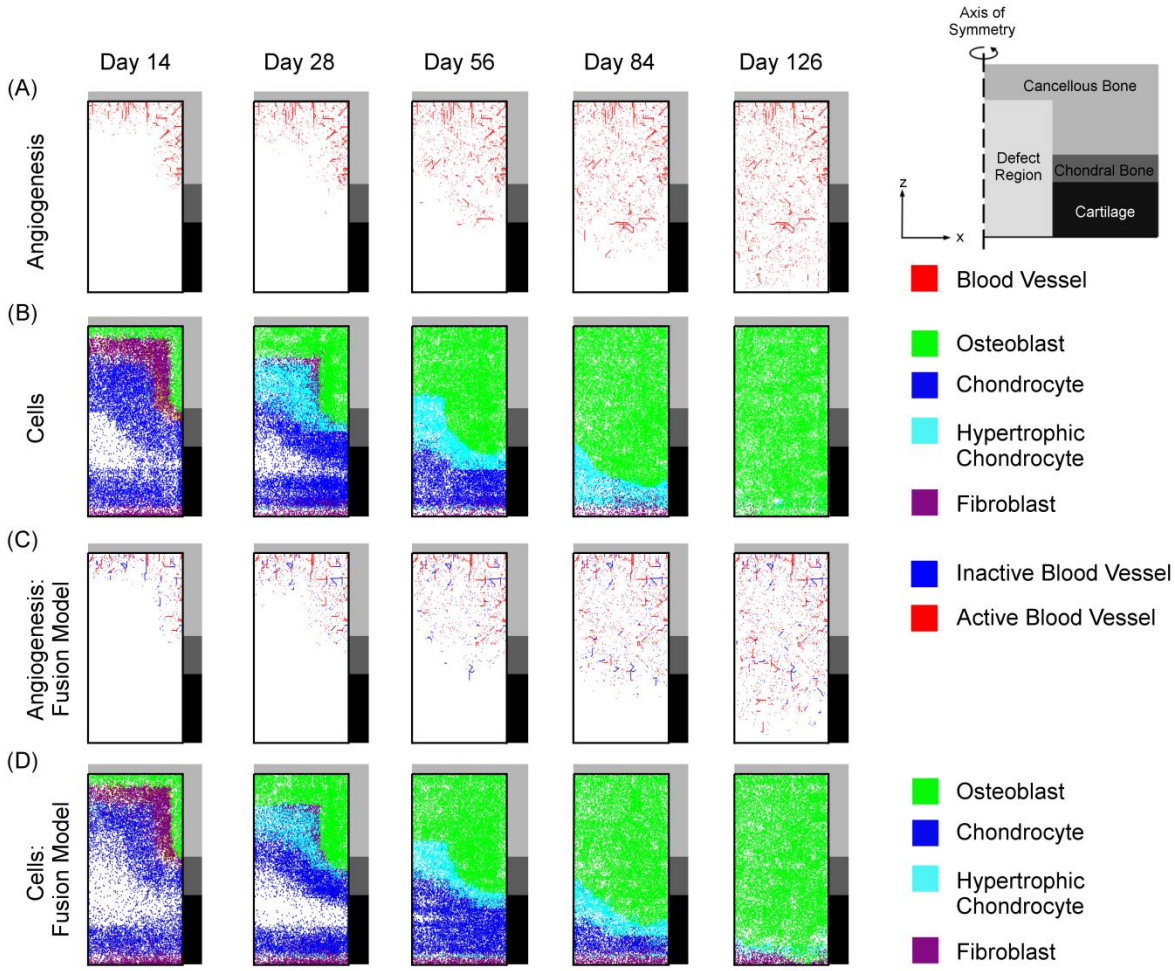


*Supplementary Figure 2: Comparison of the vascular network and course of cell differentiation predicted at Days 14, 28, 56, 84 and 126, obtained using the early model of angiogenesis where all vessels were considered active (A, B), and the updated model of angiogenesis where vessels had to form a closed loop before they were considered active (C, D).*

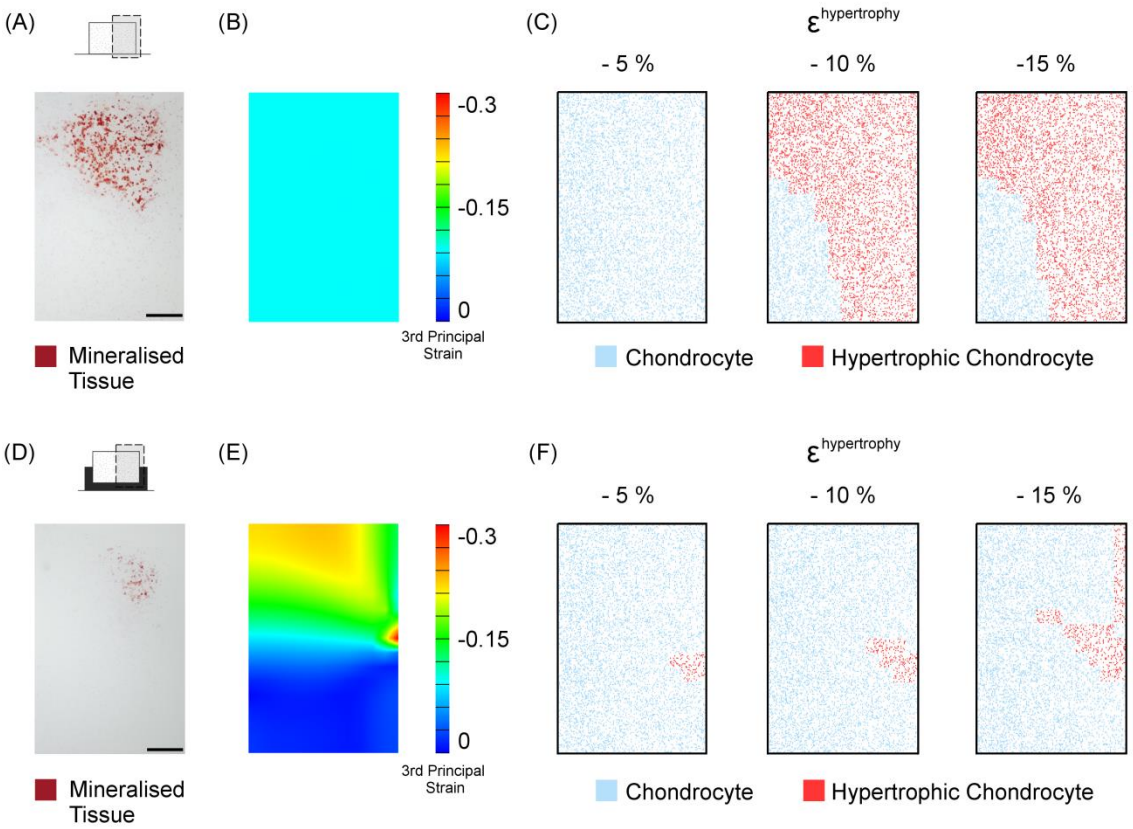


*Supplementary Figure 3: Experimental and simulation results of the In vitro DC groups. Alcian red staining was used to determine the spatial arrangement of calcific deposition (and chondrocyte hypertrophy) in the (A) unconfined and (C) confined groups following 28 days of DC. These were compared to the predicted spatial distribution of chondrocyte hypertrophy from the (B) unconfined and (D) confined in silico models of the DC groups for different values of $\varepsilon^{hypertrophy}$ where hypertrophy was inhibited by the 3$^{rd}$ principal strain.*

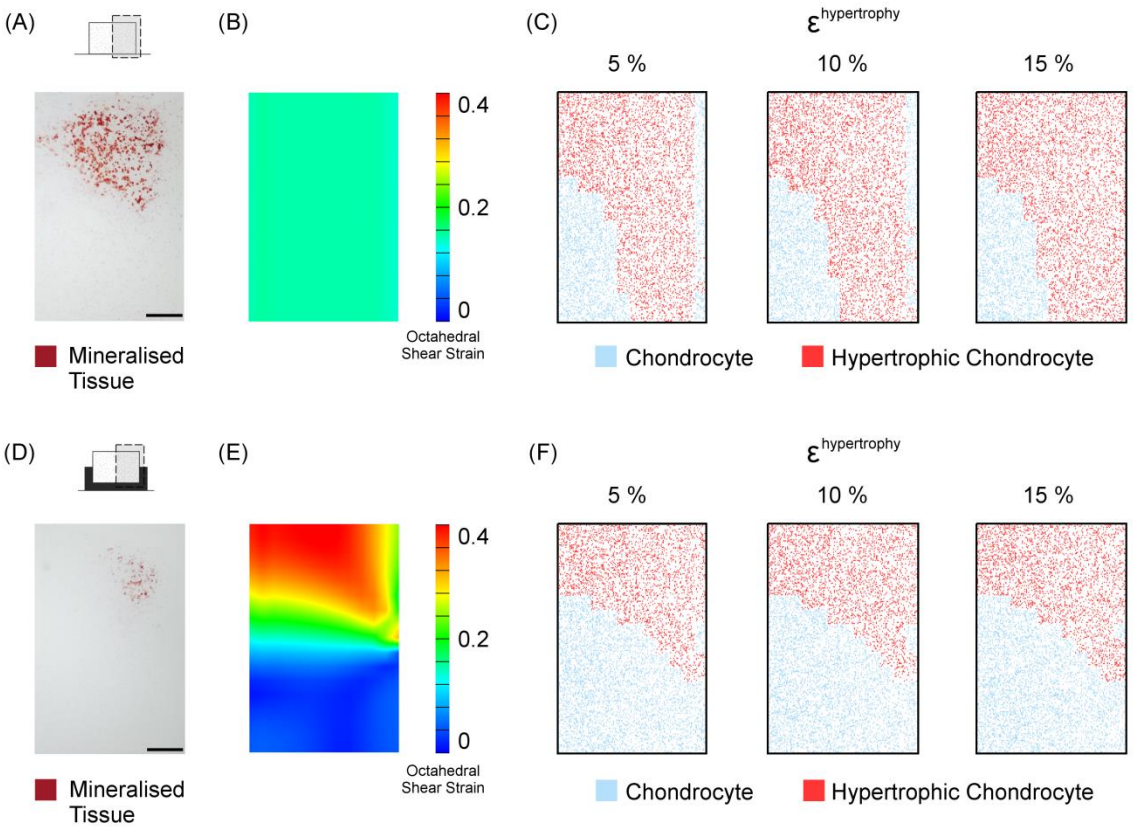


*Supplementary Figure 4: Experimental and simulation results of the In vitro DC groups. Alcian red staining was used to determine the spatial arrangement of calcific deposition (and chondrocyte hypertrophy) in the (A) unconfined and (C) confined groups following 28 days of DC; These were compared to the predicted spatial distribution of chondrocyte hypertrophy from the (B) unconfined and (D) confined in silico models of the DC groups for different values of* $\varepsilon^{hypertrophy}$ where hypertrophy was inhibited by a combination of the hydrostatic strain and the octahedral shear strain.

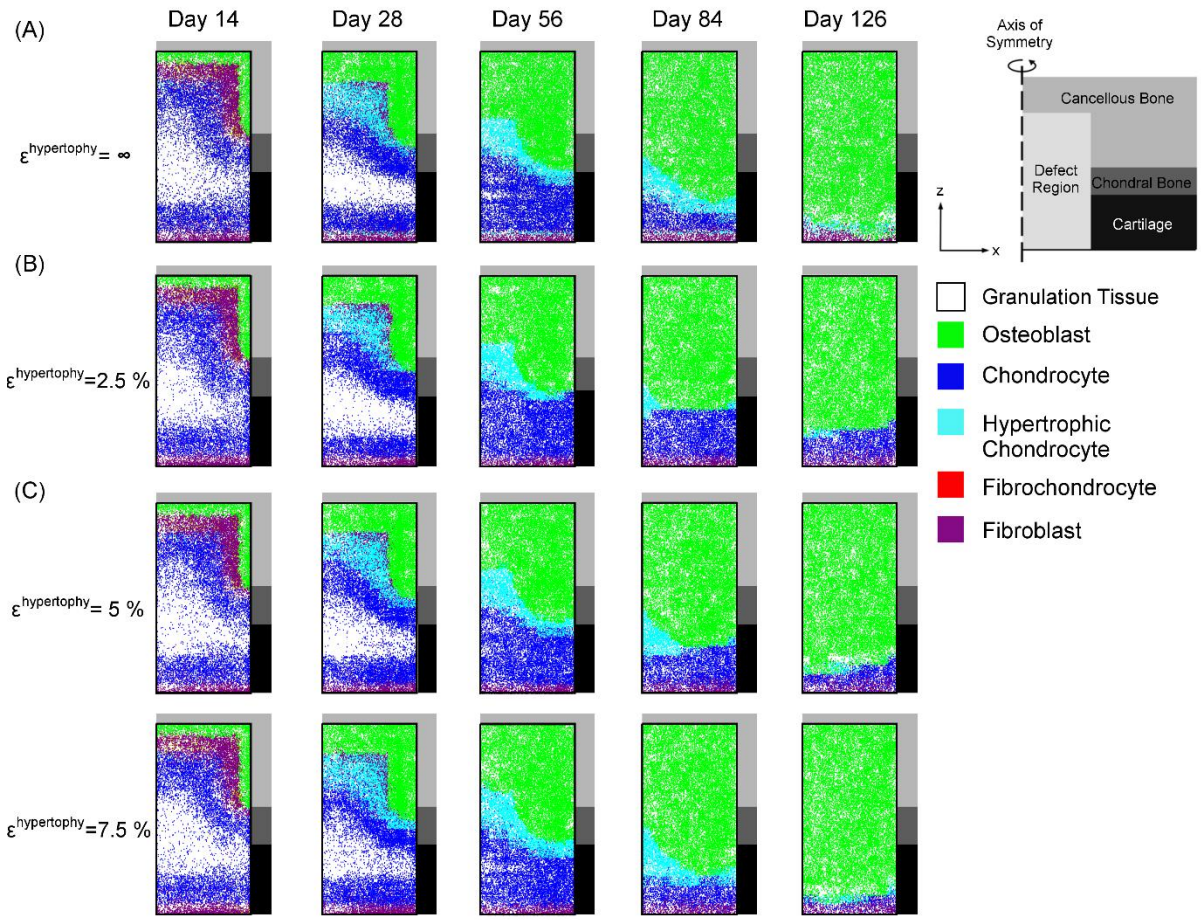


*Supplementary Figure 5: Model predictions of cell differentiation at different times during the spontaneous repair of an osteochondral defect using the: (A) previous tissue differentiation algorithm where chondrocyte hypertrophy was regulated solely by the oxygen tension (B – D) The updated algorithm where chondrocyte hypertrophy was regulated by the oxygen tension and the 3rd principal strain. The parameter $\varepsilon^{hypertrophy}$ was varied between (B) 2.5 %, (C) 5 % and (D) 7.5 %.*

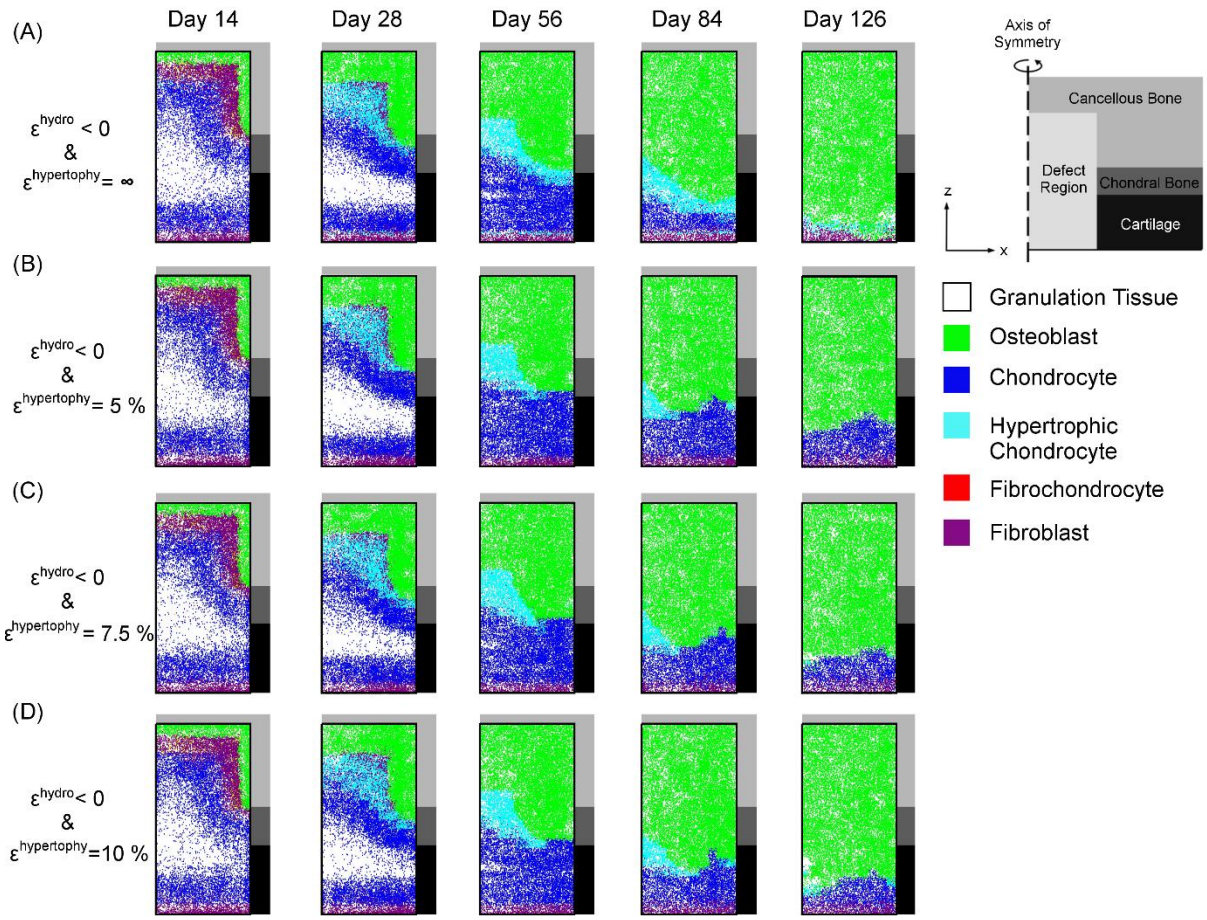


*Supplementary Figure 6: Model predictions of cell differentiation at different times during the spontaneous repair of an osteochondral defect using: (A) our previous tissue differentiation algorithm where chondrocyte hypertrophy was regulated solely by the oxygen tension (B – D) an updated algorithm where chondrocyte hypertrophy was regulated by the oxygen tension, the hydrostatic strain and the octahedral shear strain. The parameter $\varepsilon^{hypertrophy}$ was varied between (B) 5 %, (C) 7.5 % and (D) 10 %.*

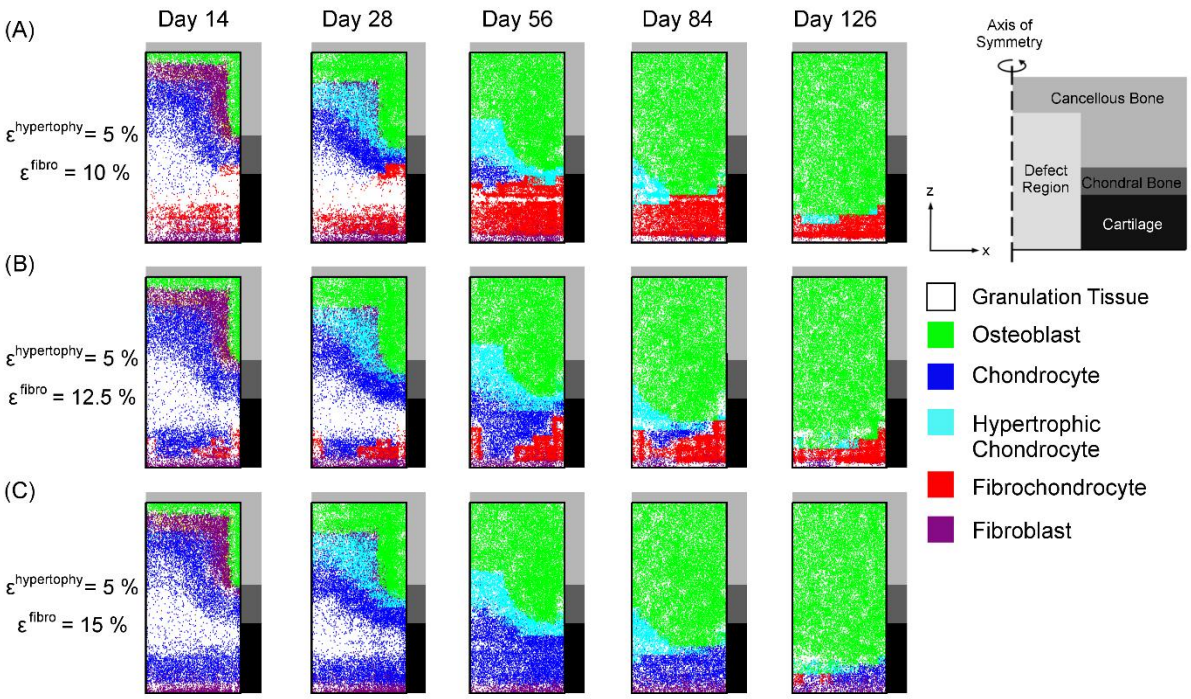


*Supplementary Figure 7: Model predictions of cell differentiation at different times during the spontaneous repair of an osteochondral defect using an updated algorithm where chondrocyte hypertrophy was regulated by the oxygen tension and the octahedral shear strain ($\varepsilon^{hypertrophy}$= 5 %) and fibrocartilage could form based on the local 1$^{st}$ principal strain. The parameter $\varepsilon^{fibrocartilage}$ was varied between (E) 2.5 %, (F) 5 % and (G) 7.5 %.*

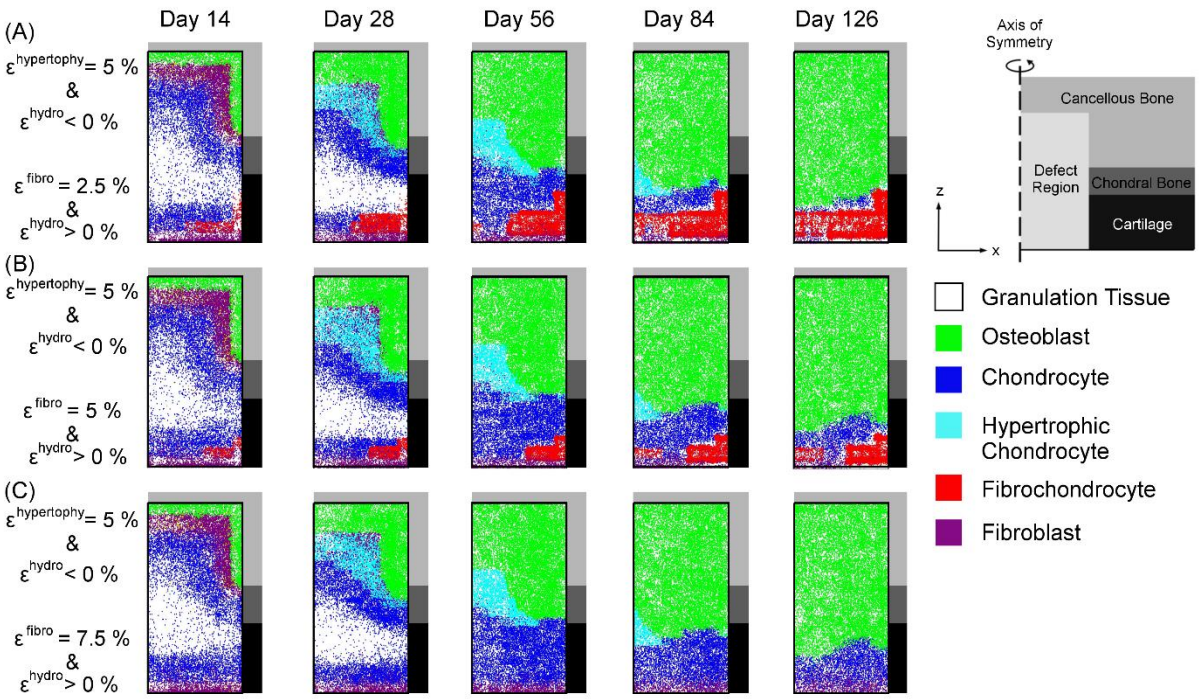


*Supplementary Figure 8: Model predictions of cell differentiation at different times during the spontaneous repair of an osteochondral defect using an updated algorithm where chondrocyte hypertrophy was regulated by the oxygen tension, the hydrostatic strain and the octahedral shear strain ($\varepsilon^{hypertrophy}$= 5 %) and fibrocartilage could form based on a combination of the local hydrostatic strain and octahedral shear strain. The parameter $\varepsilon^{fibrocartilage}$ was varied between (E) 10 %, (F) 12.5 % and (G) 15 %.*